Published in final edited form as:
Nature. 2020 November 01; 587(7835): 657–662. doi:10.1038/s41586-020-2601-5.

Papain-like protease regulates SARS-CoV-2 viral spread and innate immunity

Donghyuk Shin[1,2,3], **Rukmini Mukherjee**[1,2], **Diana Grewe**[2], **Denisa Bojkova**[4], **Kheewoong Baek**[5], **Anshu Bhattacharya**[1,2], **Laura Schulz**[6], **Marek Widera**[4], **Ahmad Reza Mehdipour**[6], **Georg Tascher**[1], **Paul P. Geurink**[7], **Alexander Wilhelm**[4,8], **Gerbrand J. van der Heden van Noort**[7], **Huib Ovaa**[7,13], **Stefan Müller**[1], **Klaus-Peter Knobeloch**[9], **Krishnaraj Rajalingam**[10], **Brenda A. Schulman**[5], **Jindrich Cinatl**[4], **Gerhard Hummer**[6,11], **Sandra Ciesek**[4,8,12], **Ivan Dikic**[1,2,3,12]

[1]Institute of Biochemistry II, Faculty of Medicine, Goethe University, Frankfurt, Germany [2]Buchmann Institute for Molecular Life Sciences, Goethe University, Frankfurt, Germany [3]Max Planck Institute of Biophysics, Frankfurt, Germany [4]Institute of Medical Virology, University Hospital Frankfurt, Frankfurt, Germany [5]Department of Molecular Machines and Signaling, Max Planck Institute of Biochemistry, Martinsried, Germany [6]Department of Theoretical Biophysics, Max Planck Institute of Biophysics, Frankfurt, Germany [7]Oncode Institute and Department of Chemical Immunology, Leiden University Medical Centre, Leiden, The Netherlands [8]Institute of Pharmaceutical Biology, Goethe-University, Frankfurt, Germany [9]Institute of Neuropathology, Faculty of Medicine, University of Freiburg, Freiburg, Germany [10]Cell Biology Unit, University Medical Center of the Johannes Gutenberg University Mainz, Mainz, Germany [11]Institute of Biophysics, Goethe University Frankfurt, Frankfurt, Germany [12]Fraunhofer Institute for Molecular Biology and Applied Ecology (IME), Branch Translational Medicine and Pharmacology, Frankfurt, Germany [13]Deceased: Huib Ovaa

Abstract

Correspondence to: Ivan Dikic.

Correspondence and requests for materials should be addressed to I.D. dikic@biochem2.uni-frankfurt.de.

Reporting summary
Further information on research design is available in the Nature Research Reporting Summary linked to this paper.

Author contributions D.S. and I.D. conceived the project. D.S. contributed protein purification, biochemical and biophysical activity assay and structure determination. R.M. performed cell biology experiments. D.G. contributed protein purification. D.B. contributed virus infection experiments, M.W. and A.W. performed RT–qPCR measurements, K.B. performed the deneddylation assay. A.B. and G.T. designed and performed mass spectrometry experiments and analysed data. L.S. and A.R.M. performed molecular dynamics simulations. K.R. contributed to RT–qPCR materials and critical advice. P.P.G. and G.J.v.d.H.v.N. synthesized Ub(l) probes and reagents in the laboratory of H.O. S.M. and K.-P.K. provided Ubl probes and reagents. B.A.S., G.H., J.C., S.C. and I.D. supervised the project. D.S. and I.D. analysed the data and wrote the manuscript with input from all co-authors.

Competing interests The authors declare no competing interests.

Peer review information *Nature* thanks Rolf Hilgenfeld, Ingrid Wertz and the other, anonymous, reviewer(s) for their contribution to the peer review of this work.

Europe PMC Funders Author Manuscripts

The papain-like protease PLpro is an essential coronavirus enzyme that is required for processing viral polyproteins to generate a functional replicase complex and enable viral spread[1,2]. PLpro is also implicated in cleaving proteinaceous post-translational modifications on host proteins as an evasion mechanism against host antiviral immune responses[3–5]. Here we perform biochemical, structural and functional characterization of the severe acute respiratory syndrome coronavirus 2 (SARS-CoV-2) PLpro (SCoV2-PLpro) and outline differences with SARS-CoV PLpro (SCoV-PLpro) in regulation of host interferon and NF-κB pathways. SCoV2-PLpro and SCoV-PLpro share 83% sequence identity but exhibit different host substrate preferences; SCoV2-PLpro preferentially cleaves the ubiquitin-like interferon-stimulated gene 15 protein (ISG15), whereas SCoV-PLpro predominantly targets ubiquitin chains. The crystal structure of SCoV2-PLpro in complex with ISG15 reveals distinctive interactions with the amino-terminal ubiquitin-like domain of ISG15, highlighting the high affinity and specificity of these interactions. Furthermore, upon infection, SCoV2-PLpro contributes to the cleavage of ISG15 from interferon responsive factor 3 (IRF3) and attenuates type I interferon responses. Notably, inhibition of SCoV2-PLpro with GRL-0617 impairs the virus-induced cytopathogenic effect, maintains the antiviral interferon pathway and reduces viral replication in infected cells. These results highlight a potential dual therapeutic strategy in which targeting of SCoV2-PLpro can suppress SARS-CoV-2 infection and promote antiviral immunity.

The novel coronavirus SARS–CoV-2 is the cause of the current worldwide outbreak of the respiratory disease coronavirus disease 2019 (COVID-19)[6]. COVID-19 generally has less severe symptoms and a lower case-fatality rate but is transmitted more rapidly compared with the related SARS-CoV, which caused the SARS outbreak in 2003. The SARS-CoV-2 genome shares high sequence identity with SARS-CoV[7,8]. Both viruses critically rely on the activity of viral proteases: the main protease (Mpro, also known as 3CLpro or non-structural protein 5 (nsp5)) and the papain-like protease (PLpro, the protease domain of nsp3) to generate a functional replicase complex and enable viral spread[1,2]. SCoV-PLpro cleaves ubiquitin and ISG15, known regulators of host innate immune pathways, and inhibition of SCoV-PLpro has been shown to block SARS-CoV replication[3–5].

SARS-CoV-2 PLpro preferentially cleaves ISG15

SCoV-PLpro and SCoV2-PLpro are closely related and diverge from Middle East respiratory syndrome (MERS) coronavirus PLpro (MERS-PLpro) (Extended Data Fig. 1a). Purified SCoV-PLpro and SCoV2-PLpro exhibit differences in their substrate preferences, as revealed by their cleavage of ubiquitin or ISG15 from substrates in HeLa cells treated with interferon-α (IFN-α) (Extended Data Fig. 1b). SCoV-PLpro strongly reduced the appearance of ubiquitinated substrates, with a lesser effect on ISGylated substrates, whereas SCoV2-PLpro preferentially reduced appearance of ISG15-conjugated (ISGylated) protein substrates (Extended Data Fig. 1b).

We next used activity-based probes, namely a highly reactive propargylamide (Prg) ‘warhead’, which forms a covalent bond with catalytic cysteines, and a 7-amido-4-methylcoumarine (AMC) probe, which emits fluorescence upon cleavage, enabling the monitoring of the kinetics of the protease activity[9–13]. SCoV2-PLpro preferentially reacted

with the ISG15–Prg probe, but showed weak activity towards K48-linked di-ubiquitin (K48-Ub_2) and Nedd8, and no activity towards SUMO-based Prg probes (Fig. 1a, Extended Data Fig. 1c). SCoV-PLpro showed highest reactivity with K48-Ub_2 Prg probes, and less reactivity towards the ISG15–Prg probe (Fig. 1a, Extended Data Fig. 1c). This substrate preference was further confirmed using competition assays with increasing doses of K48-Ub_2 (Extended Data Fig. 1d, e). In the reaction with SCoV-PLpro, K48-Ub_2 effectively competed with both ISG15–Prg and ISG15–AMC, whereas competitive displacement was much less effective with SCoV2-PLpro. We also examined the catalytic efficiency (turnover number (k_{cat})/Michaelis constant (K_m)) of both PLpro proteins (Fig. 1b, Extended Data Table 2), which indicated that SCoV2-PLpro cleaved AMC from ISG15–AMC more efficiently than from K48-Ub_2–AMC, whereas SCoV-PLpro cleaved AMC from K48-Ub_2 more efficiently. Of note, the apparent catalytic efficiencies (k_{cat}/K_m) of the two PLpro enzymes towards ISG15 were similar, but SCoV2-PLpro showed slightly higher specificity towards ISG15 (indicated by lower K_m) (Fig. 1b, Extended Data Table 2). Consistently, SCoV2-PLpro bound ISG15 with a 20-fold higher affinity compared with K48-Ub_2, whereas SCoV-PLpro bound K48-Ub_2 with a 10-fold higher affinity compared with both mouse and human ISG15[14] (Fig. 1c, Extended Data Table 3). Indeed, the deISGylase activity of SCoV2-PLpro towards Prg- or AMC-based substrates, was similar to or higher than that of mouse USP18, a specific deISGylase[12,15] (Extended Data Fig. 1f, g). Both PLpro enzymes also displayed weak deneddylation activity towards hyperneddylated CUL1, a common feature of dened-dylases such as DEN1 (Extended Data Fig. 1c, h, i). Together, these results indicate that SCoV2-PLpro preferentially cleaves ISG15 from substrates over ubiquitin chains and Nedd8 in vitro, whereas SCoV-PLpro targets ubiquitin chains and, to a lesser extent, ISG15 and Nedd8 (Fig. 1d).

Structural analysis of SCoV2-PLpro–ISG15

To gain insight into the molecular basis underlying specificity of SCoV2-PLpro–ISG15, we determined the crystal structure of a complex comprising SCoV2-PLpro(C111S) and mouse ISG15 (Fig. 2a, Extended Data Fig. 2a). Notably, ISG15 displays two tandem ubiquitin-like folds. The overall assembly of SCoV2-PLpro and the two ISG15 domains was similar to the complex of MERS-PLpro with human ISG15 complex[16] (Protein Data Bank (PDB) ID: 6BI8; Extended Data Fig. 2a). The catalytic cysteine residue is also conserved in SARS (Extended Data Fig. 2b). Compared with the crystal structure of ISG15 in isolation (PDB ID: 5TLA)[17], the N-terminal half of ISG15 is rotated by almost 90° and rests on the S2 helix of SCoV2-PLpro (Fig. 2b). The structure of SCoV-PLpro in complex with the C terminus of mouse ISG15 (PDB ID: 5TL7)[17] showed that SCoV-PLpro and SCoV2-PLpro share the same binding mode to the C-lobe of mouse ISG15 (Extended Data Fig. 2c). We next compared the structure of the SCoV2-PLpro–ISG15 complex to that of SCoV-PLpro bound to K48-Ub_2, in which the proximal ubiquitin is linked to the catalytic site. The main difference between these complexes is an interaction remote from the catalytic site, in which a protease S2 site binds the distal ubiquitin in the K48-linked chain, or the N-terminal ubiquitin-like fold in ISG15. Whereas SCoV-PLpro Leu76 mediates a hydrophobic interaction with Ile44 on ubiquitin, the corresponding residue on SCoV2-PLpro is Thr75 (Fig. 2c). To mimic the hydrophobic interaction observed in SCoV-PLpro, we generated two

variants of SCoV2-PLpro (T75A and T75L). The T75L mutant, but not T75A, resulted in a K48-Ub_2–AMC cleavage (Fig. 2d). This indicates that the presence and size of the hydrophobic residue at this site are critical determinants for ubiquitin binding. We also compared papain-like proteases from other coronaviruses, including the common human coronaviruses OC43, 229E and NL63 (Extended Data Fig. 3). The S2 binding site in papain-like proteases is poorly conserved across coronaviruses and exhibits variable hydrophobicity at the position corresponding to Thr75 of SCoV2-PLpro, which might influence substrate specificity.

Next, we examined whether other residues in SCoV2-PLpro contribute to its enhanced affinity for ISG15. SCoV2-PLpro Val66 faces the hydrophobic patch (Ala2, Thr20 and Met23) on the N-terminal ubiquitin fold domain of ISG15 (Fig. 2e). Both PLpro enzymes share Phe (SCoV2-PLpro Phe69 and SCoV-PLpro Phe70) as the core residue mediating hydrophobic interactions with either ubiquitin or ISG15. Mutating Phe69 (F69A) or Val66 (V66A) on SCoV2-PLpro decreased its enzymatic activity and showed slower reaction with ISG15-Prg compared to the wild type (Fig. 2f).

The interaction between SCoV2-PLpro and K48-Ub_2 and mouse ISG15 was also examined using molecular dynamics simulations (Extended Data Fig. 2d, e). Multi-microsecond molecular dynamics simulations confirmed that SCoV2-PLpro interacts more tightly with ISG15 compared with K48-Ub_2 (reconfirming K_d values measured in Fig. 1e). In three independent runs of 3.2 μs, ISG15 remained bound as in the SCoV2-PLpro–ISG15 X-ray structure. By contrast, the distal ubiquitin of K48-Ub_2 separated from SCoV2-PLpro in four out of six runs on a microsecond time scale. We identified L75T to be the differentiator between K48-Ub_2 and SCoV-PLpro, as it weakens the hydrophobic cluster within the binding interface. We observed that water transiently enters between K48-Ub_2 Ile44 and SCoV2-PLpro Thr75 before dissociation. Indeed, in simulations of the SCoV-PLpro double mutant (S67V/L76T) with K48-Ub_2, a similar water-mediated dissociation mechanism was observed (Extended Data Fig. 2f, g). Together, these results suggest that the S2 region determines substrate specificity and that SCoV2-PLpro shows a relative preference towards ISG15.

GRL-0617 is an inhibitor of SCoV2-PLpro

Given the urgency to identify novel therapeutic strategies against COVID-19, we tested the effect of GRL-0617, a non-covalent inhibitor of SCoV-PLpro[18], on SCoV2-PLpro (Fig. 3a). GRL-0617 was developed as an inhibitor of SCoV-PLpro and does not inhibit other host proteases[18,19]. On the basis of the binding mode of GRL-0617 and other naphthalene-based inhibitors to SCoV-PLpro[18–21], we postulated that the conserved Tyr268 of SCoV2-PLpro could also bind GRL-0617 and block the entry of the ISG15 C terminus towards the catalytic cleft of the protease (Fig. 3b, Extended Data Fig. 4a–c). Indeed, the half maximal inhibitory concentration (IC_{50}) of GRL-0617 for SCoV2-PLpro was similar to the one for SCoV-PLpro (Fig. 3c, Extended Data Fig. 4d, e). GRL-0617 is ineffective against MERS-PLpro[22]; we hypothesized that this could be due to the presence of Thr instead of Tyr at this conserved position (Tyr268 in SCoV2-PLpro) (Extended Data Fig. 3a). Accordingly, the mutation of Tyr268 to either Thr (Y269T) or Gly (Y268G) in SCoV2-PLpro strongly

reduced the inhibitory effect of GRL-0617 (Fig. 3c, Extended Data Fig. 4d, e), indicating the critical role of Tyr268 in this process. Molecular dynamics simulations of GRL-0617 with SCoV-PLpro and SCoV2-PLpro further confirmed a common binding mode between GRL-0617 and Tyr268 (Tyr269 in SCoV-PLpro) (Extended Data Fig. 4b, c).

To assess the potential therapeutic value of GRL-0617 against COVID-19, we tested the effect of GRL-0617 on the deISGylase or deubiquitinase activities of SCoV2-PLpro on host proteins. GRL-0617 effectively blocked SCoV2-PLpro activity, leading to increased levels of ISGylated proteins in lysates of IFN-α-treated cells (Extended Data Fig. 4f). GRL-0617 also blocked the deubiquitination activity of SCoV-PLpro (Extended Data Fig. 4f). Of note, the effects of GRL-0617 on the reaction between Prg probes with SCoV2-PLpro were more prominent with $ISG15_{C\text{-}term}$–Prg than $ISG15_{FL}$–Prg or ubiquitin versus K48-Ub_2 to SCoV-PLpro (Extended Data Fig. 4g, h), which is consistent with the structural data indicating that the ISG15 N-terminal ubiquitin-fold domain potentiates the interaction with SCoV2-PLpro. These results showed that GRL-0617 inhibits both SCoV2-PLpro and SCoV-PLpro.

PLpro regulates IFN and NF-κB pathways

To understand the differences in the pathophysiological roles of SCoV2-PLpro and SCoV-PLpro, and to expand our knowledge of the SARS-CoV-2 protein interaction map[23], we analysed the cellular inter-actome of both proteins. ISG15 was significantly enriched in complexes with a catalytically inactive version of SCoV2-PLpro (C111S), whereas a SCoV-PLpro mutant (C111S) predominantly associated with ubiquitin (Fig. 4a, b). In mammalian cells treated with type I IFNs (IFN-α), unconjugated ISG15 and ISG15-positive smears (probably representing ISGylated substrates) on western blots were more pronounced in immunoprecipitates of GFP-SCoV2-PLpro(C111S) than those of GFP-SCoV-PLpro(C111S) (Fig. 4c). GRL-0617 treatment blocked this association (Fig. 4c). Moreover, these closely related PLpro enzymes associate with distinct and specific sets of host proteins (Fig. 4a). For SCoV2-PLpro, these interactions include PRKDC (associated with induction by type I interferons[24]), heterogenous nuclear ribonucleo-protein K (HNRNPK; involved in host RNA splicing, a process essential for SARS-CoV-2 replication in cells[25]) and galectin1, which can induce viral fusion with target cells during HIV infection[26] (Fig. 4a). By contrast SCoV-PLpro strongly associates with several serine protease inhibitors (serpins), including serpin B3, which has been proposed to inhibit papain proteases[27,28]. Co-expression of serpin B3 with PLpro enzymes partially restored NF-κB signalling in cells expressing SCoV-PLpro, but had no effect on SCoV2-PLpro regulation of the IFN pathway (Extended Data Fig. 5a, b).

Consistently, expression of SCoV2-PLpro and SCoV-PLpro in mammalian cells decreased ISGylation of cellular proteins following IFN-α stimulation (Extended Data Fig. 5c), including ISGylation of interferon regulatory factor 3 (IRF3), a critical component in the type 1 interferon pathway[29]. Both SCoV2-PLpro and SCoV-PLpro reduced IRF3 ISGylation, with SCoV2-PLpro having a more potent effect (Fig. 4d). Decreases in phosphorylation of TBK1 and IRF3, and nuclear translocation of IRF3 were detected upon expression of SCoV-PLpro or SCoV2-PLpro (Extended Data Fig. 5d, e). SCoV2-PLpro(C111S) showed stronger dominant negative effects on IRF3 phosphorylation

compared with SCoV-PLpro(C111S) (Extended Data Fig. 5d, e). TBK1 phosphorylation also activates the NF-κB pathway, causing upregulation of inflammatory signalling[30]. Although expression of SCoV-PLpro had less effect on IRF3 ISGylation (Fig. 4d), it strongly attenuated degradation of IκB-α (Extended Data Fig. 5f, g). SCoV-PLpro also caused a severe reduction in nuclear translocation of p65 in cells treated with TNF (Extended Data Fig. 5h).

Sensing of viral nucleic acids is mimicked by poly(I:C) treatment, which induces IFN-β expression[31]. Expression of SCoV2-PLpro more effectively decreased the activation of the *IFNB1* promoter compared with SCoV-PLpro following poly(I:C) treatment. This inhibitory effect of both PLpro enzymes was neutralized by GRL-0617 treatment (Extended Data Fig. 6a, c). By contrast, expression of SCoV-PLpro predominantly blocked TNF-induced NF-κB p65 expression, also in a GRL-0617-dependent manner (Extended Data Fig. 6b, d). Together, we show how two closely related coronaviruses (SARS and SARS-CoV-2) differentially counteract the host immune system using their PLpro enzymes.

Role of PLpro in viral spread and IFN responses

GRL-0617 has been shown to inhibit viral replication of SARS-CoV[18]. Thus, to determine whether inhibiting SCoV2-PLpro can also block SARS-CoV-2 replication, we infected CaCo-2 cells with SARS-CoV-2 and treated them with GRL-0617 (Fig. 5a). The effect of GRL-0617 was measured by inhibition of cytopathogenic effect (CPE). We observed a gradual dose-dependent inhibition of SARS-CoV-2-induced CPE in the presence of GRL-0617, with 100 μM GRL-0617 almost completely inhibiting CPE (Fig. 5b). In addition, GRL-0617 treatment reduced active viral replication (SARS-CoV-2 subgenomic RNA4-encoding E gene), as measured by genetic monitoring of the intracellular production of viral RNA (Fig. 5c). Consequently, a decrease in the release of viral particles from infected cells into the supernatant was also observed upon GRL-0617 treatment (Fig. 5d, Extended Data Fig. 7a). This suggests that inhibition of SCoV2-PLpro by GRL-0617 impedes viral replication, thereby attenuating the ongoing viral RNA synthesis.

Having demonstrated a role for expression of SCoV2-PLpro and SCoV-PLpro in attenuating host antiviral IFN pathways, we anticipated that inhibition by GRL-0617 would reverse this process. Indeed, GRL-0617 treatment of SARS-CoV-2-infected cells led to a marked increase in IRF3 ISGylation (Fig. 5e), which has previously been shown to regulate antiviral immune response[32]. Moreover, phosphorylation of IRF3 and TBK1, markers for IFN pathway activation, and p65 phosphorylation, used to monitor NF-κB pathway activation, were increased in SARS-CoV-2-infected cells upon GRL-0617 treatment (Fig. 5f). Notably, GRL-0617 treatment significantly rescued the expression of IFN-responsive genes (*ISG15*, *OAS1*, *PKR* (also known as *EIF2AK2*)) and *MX1*) in SARS-CoV-2-infected cells (Fig. 5g, Extended Data Fig. 7b). These findings provide evidence that inhibition of SCoV2-PLpro, in addition to blocking viral RNA synthesis, can also increase antiviral signalling via TBK1 and IRF3 (Extended Data Fig. 7c). Although experiments conducted with GRL-0617 provide evidence supporting the therapeutic value of pharmacologically targeting SCoV2-Plpro in patients, the low potency of GRL-0617 suggests that additional studies are needed to develop more potent and selective PLpro inhibitors.

Finally, we tested changes in CaCo-2 cells upon infection with SARS-CoV and SARS-CoV-2. GRL-0617 treatment of infected cells showed an overall similar pattern in biochemical and transcriptional parameters of the type I IFN and NF-κB pathways (Fig. 5e–g). However, we found that GRL-0617 was consistently more effective in restoring ISGylation and phosphorylation level of IRF3 and expression of IFN-responsive genes upon infection with SARS-CoV-2 compared with SARS-CoV (Fig. 5e–g). By contrast, transcription levels of the proinflammatory cytokines IL-6 and IL-8 appeared similar between SARS-CoV and SARS-CoV-2 in this epithelial cell culture model (Fig. 5g). Consistent with these observations, a recent study has shown that SARS-CoV-2 infection in animal models and in human patients with COVID-19 is correlated with low IFN type I and type III responses[33]. Although preferential deISGylation activity of SCoV2-PLpro may contribute to decreased type I IFN signalling, more detailed studies are needed to understand the key regulatory factors contributing to innate and adaptive immunity that control the distinct pathologic outcomes of SARS-CoV and SARS-CoV-2 infections[34].

In summary, this study provides mechanistic understanding of the functions of SCoV2-PLpro during SARS-CoV-2 infection and establishes SCoV2-PLpro as a promising target for therapeutic intervention against COVID-19. Recent reports of newly identified inhibitors of SCoV2-PLpro[35–37] could lead to the rapid development of novel anti-COVID-19 therapeutics with dual effects—blocking SARS-CoV-2 spread and promoting antiviral immunity in the host. Furthermore, the main protease of SARS-CoV-2 has been in focus as a potential drug target against COVID-19 and several novel inhibitors have already been described[38–40]. Combining drugs targeting essential SARS-CoV-2 proteases (PLpro and/or main protease) with drugs targeting SARS-CoV-2 RNA-dependent polymerase may offer successful therapeutic options in future[41].

Online content

Any methods, additional references, Nature Research reporting summaries, source data, extended data, supplementary information, acknowledgements, peer review information; details of author contributions and competing interests; and statements of data and code availability are available at https://doi.org/10.1038/s41586-020-2601-5

Methods

No statistical methods were used to predetermine sample size. The experiments were not randomized. The investigators were not blinded to allocation during experiments and outcome assessment.

Plasmids construction

The papain-like protease domain sequence was obtained from the SARS-CoV-2 complete genome (NCBI genome databank, Severe acute respiratory syndrome coronavirus 2 isolate Wuhan-Hu-1, complete genome; NC_045512). Protein sequence for CoV2 PLpro Ubl domain (amino acids, 746–1060) of Nsp3 protein from SARS-CoV-2 (Nsp3; YP_009725299.1) was codon optimized, synthesized and cloned into pET28b with NcoI and XhoI to have C-terminal His-tag (Genescript). Protein sequences of the PLpro-Ubl domain

of SARS and MERS (PDB ID: 3MJ5 and 5W8U, respectively[20,42]) were also codon optimized, synthesized and cloned into pET28b with NcoI and XhoI to add C-terminal His tags (Genescript). Mutants were generated by PCR and verified by sequencing. For mammalian expression, PLpros were cloned into pEGFP-C1 (clontech). To produce the vector pACE-ISG15, a synthetic cDNA was used for murine ISG15 (residues 1–155) with an added N-terminal His_6 tag and the recognition site for the HRV-3C protease (Mr. Gene).

Protein purification

BL21(DE3) *Escherichia coli* competent cells (NEB) were transformed with plasmids and grown in LB medium to an OD600 of 0.6–0.8 at 37 °C. Protein production was induced by addition of 0.5 mM isopropyl-d-thiogalactopyranoside (IPTG) and 1 mM zinc chloride ($ZnCl_2$). The cells were further grown overnight at 18 °C and collected. The cell pellet was resuspended in lysis buffer (50 mM Tris-HCl, 150 mM NaCl, 10 mM Imidazole, 2 mM DTT, pH 8.5) and lysed by sonication and centrifuged at 13,000 rpm to clarify the supernatant. The supernatant was incubated 2 h with TALON beads (Takara) pre-equilibrated with lysis buffer and non-specific proteins were cleared with washing. Proteins were eluted with elution buffer (50 mM Tris-HCl, 150 mM NaCl, 250 mM imidazole, 2 mM DTT, pH 8.5). Eluted proteins were buffer exchanged to storage buffer (20 mM Tris-HCl, 100 mM NaCl, 2 mM DTT, pH 8.5) and stored for biochemical analysis. For crystallization of SCoV2-PLpro(C111S), the cell pellet was resuspended in lysis buffer (50 mM Tris-HCl, 150 mM NaCl, 10 mM imidazole, 1 mM TCEP, pH 7.4) and lysed by sonication and centrifuged at 13,000 rpm to clarify the supernatant. The supernatant was incubated 2 h with TALON beads (Takara) pre-equilibrated with lysis buffer and non-specific proteins were cleared with washing. Proteins were eluted with elution buffer (50 mM Tris-HCl, 150 mM NaCl, 250 mM imidazole, 1 mM TCEP, pH 7.4) and further purified on size-exclusion column (Superdex 75 16/60, GE Healthcare) pre-equilibrated with 20 mM Tris-HCl, 100 mM NaCl, 1 mM TCEP, pH7.4. Proteins were concentrated to 20 mg ml^{-1} and stored for crystallization. For the expression of mouse ISG15, BL21(DE3) *E. coli* competent cells (NEB) were transformed with pACE-ISG15. A single bacterial colony was picked and transferred in 5 ml DYT medium with 0.2% (w/v) glucose and 100 μg ml^{-1} ampicillin and grown overnight at 37 °C. The preculture was centrifuged for 3 min at 3,000*g* centrifuged and resuspended in 5 ml of fresh medium. Two litres of DYT medium was mixed with 5 ml of the pre-culture and grown at 37 °C until it reached an OD600 of 0.6. Protein expression was induced by adding IPTG (final concentration 1 mM). The cells were grown for 20 h at 28 °C and collected by centrifugation (10 min, 5,000*g*, 4 °C). Five grams of *E. coli* pellet (ISG15 or ISG15(C76S)) were thawed on ice and resuspended in 30 ml of buffer A-ISG15 (50 mM Na_2HPO_4, 500 mM NaCl pH 7.0, 1 protease inhibitor tablet (Roche)). The cells were disrupted using a French press and the lysate was centrifuged for 1 h 40,000*g* and 4 °C. All cleaning steps were carried out with an ÄkTA chromatography system (GE Healthcare) at 4 °C. The supernatant was applied to a 15 ml Ni-FF Sepharose column (GE Healthcare). The column was filled with 4 column volumes of 50 mM Na_2HPO_4, 500 mM NaCl, 15 mM imida-zole pH 7.0, washed and the protein was eluted with a linear imidazole gradient over 20 column volumes and final imidazole concentration of 500 mM (buffer B-ISG15). About 30 mg of the eluted protein was treated with 1 mg His_6–HRV-3C and dialysed against buffer A-ISG15 at 16 °C for 16 h. The protein was then applied to the same column containing the

protein, concentrated to about 6 mg ml^{-1} and further purified with a size-exclusion column (Superdex 75 16/60, GE Healthcare) pre-equilibrated with 20 mM Tris-HCl, 100 mM NaCl, 1 mM TCEP, pH7.4.

Ubiquitin, NEDD8, SUMO and ISG15 activity-based probe assay

PLpro proteins were diluted (2 μM final concentration) with activation buffer (25 mM Tris-HCl pH 7.5, 150 mM NaCl, 10 mM DTT) and incubated for 10 min at 25 °C. and the activity-based probes were diluted (0.2 mg ml^{-1} final concentration) in dilution buffer (50 mM Tris-HCl 7.5, 150 mM NaCl). The reaction mixture was prepared by mixing equal volume of activated PLpro proteins (2 μM) and activity-based probes (0.2 mg ml^{-1}). Reactions were conducted at indicated temperature (on ice (0 °C) or 37 °C) and samples were taken at the indicated time points and the reactions were quenched by the addition of SDS sample buffer. Samples were further analysed by SDS–PAGE and stained with a silver staining kit (Thermo Fisher).

AMC probe-based kinetic assay

For determination of enzyme kinetics (k_{cat} and K_m), ubiquitin–AMC or ISG15–AMC was used as substrate of PLpro or mouse USP18 and the release of AMC was measured by increase of fluorescence (excitation/emission, 360/487 nm) on a 384-well microplate reader (PHERAstar FSX, BMG Labtech). Fvie microlitres of solution containing different concentration of K48-Ub_2–AMC (76–0 μM) or ISG15–AMC (40–0 μM) were aliquoted into 384 well plate and reaction was initiated by addition of 5 μl of PLpro or mouse USP18 (20 nM) to the well. Initial velocities of AMC release were normalized to a standard curve and the velocity versus substrate concentration plot were further analysed by Michaelis–Menten enzymatic kinetics, using the k_{cat} function with fixed value of total enzyme concentration as provided above. The experiment was repeated at least three times.

Bio-layer interferometry

Binding kinetics were determined with the OctetRed system (Fortebio). Either SCoV2-PLpro(C111S) or SCoV-PLpro(C111S) at 1 μM were loaded onto an Ni-NTA biosensor and equilibrated with binding buffer for the baseline. To examine the association rate, equilibrated sensors were transferred into solutions containing various concentration of K48-Ub_2 (90–0 μM), human ISG15 (3–0 μM) or mouse ISG15 (90–0 μM). Dissociation of PLpro was initiated by placing the sensor into reaction buffer. Values of association rate constant (k_{on}), dissociation rate constant (k_{off}) and dissociation constant (K_d) values were calculated by Octet Data analysis software (ForteBio).

Crystallization

Equal amounts of SCoV2-PLpro(C111S) and full-length murine ISG15 were mixed, giving a final concentration of 250 μM. Protein mixtures were screened with sitting-drop matrix screens in a 96-well plate with 100 nl of protein and 100 nl of precipitant solution at 293 K. Initial crystals appeared from solution containing 20% PEG 3350, 200 mM potassium thiocyanate with 125 μM protein. To optimize the crystallization condition, we diluted the protein to vary the concentration, and the diffraction-quality crystals were grown in

optimized solution containing 18% PEG 3350, 100 mM bis-tris propane pH 6.5, 200 mM potassium thiocyanate with 100 μM protein.

Data collection, processing and structure determination

Crystals were cryo-protected using mother liquor solution supplemented with 25% (v/v) ethylene glycerol. Diffraction data were collected on single frozen crystal in a nitrogen stream at 100 K at 1.00001 Å in the X06SA beamline at the Swiss Light Source, Villigen. Initial data sets were processed using XDS[43], and phases were determined by Phaser molecular replacement in ccp4 module with SCoV2-PLpro and mouse ISG15 as the template model[44]; PDB IDs: 6W9C and 5TLA). Structure refinement and manual model building were performed with Coot and Phenix.Refine[45,46] (Extended Data Table 1). There were 93.26% and 6.74% of the residues in the favoured and allowed regions of the Ramachandran plot respectively, and no residues were found in disallowed regions.

Cell lysates, deubiquitination and deISGylation assay

HeLa or A549 cells were treated with IFN-α (200 U ml^{-1}) for 48 h to induce ISGylation. Cells were lysed with lysis buffer (50 mM Tris-HCl (pH 8.0), 150 mM NaCl, 1% (v/v) NP-40) and concentration was measured with the BCA assay (Thermo Fisher). Ten micrograms of lysates were incubated with 100 nM of PLpro for indicated time points at 37 °C and analysed by immunoblotting with indicated antibodies. To test the inhibitory effect of GRL-0617, 40 μM of GRL-0617 was included during the reaction. Images were obtained using Image lab software (Bio-Rad).

Deneddylation and IκBα deubiquitination assay

All proteins described are of human origin. CUL1–RBX1, SKP1–β-TRCP2, UBE2M, UBE2D3, NEDD8, UB, APPBP1–UBA3 and UBA1 were purified as previously described[47]. Neddylated CUL1–RBX1 was generated as previously described[47]. The reaction for generating hyperneddylated CUL1–RBX1 was driven at pH 8.8 at 37 °C for 30 min and purified by size exclusion chromatography. The USP2 catalytic core was purified with nickel affinity chromatography, liberated of the His tag by overnight thrombin cleavage, followed by ion exchange and size-exclusion chromatography. Den1 was purified by GST affinity chromatography, liberated of the GST tag by overnight TEV cleavage, followed by ion exchange and size-exclusion chromatography. The Cop9 signallosome (CSN) was purified as previously described[48]. Deneddylation assays were performed with 1 μM hyperneddylated CUL1–RBX1, and 5μM protease (SCoV-PLpro, SCoV2-PLpro, DEN1 and USP2) or 20 nM CSN. The reaction was performed at 37 °C in 2 5mM Tris 100 mM NaCl, 5 mM DTT pH 8.5, and in the case of CSN, with and additional 10 mM $MgCl_2$. Samples were taken at each indicated time point and quenched with 2× SDS–PAGE sample buffer. Gels were stained by Coomassie blue and scanned on an Amersham imager 600. IκBα deubiquitylation assays were performed by first generating a ubiquitylated IκBα, with 200 nM UBA1, 1 μM UBE2D3, 20 μM UB, 500 nM neddylated CRL1–β-TRCP, and 5 μM fluorescently labelled IκBα at 37 °C in 50 mM Tris, 50mM NaCl, 10mM $MgCl_2$, 5mM DTT pH 7.5 for 30 min. Reaction was quenched by adding 80 mM EDTA for 5 min. The deubiquitylation reaction was started by mixing 3 μM of protease (SCoV-PLpro, SCoV2-PLpro or USP2) with the ubiquitylation reaction, and samples were taken at each time point

Europe PMC Funders Author Manuscripts

and quenched with 2× SDS–PAGE sample buffer. Gels were scanned on an Amersham Typhoon (GE) detecting the fluorescently labelled IκBα.

Molecular dynamics simulations

SCoV-PLpro (wild type and double mutant) and SCoV2-PLpro with K48-Ub_2 — The coordinates of SCoV-PLpro with bound K48-Ub_2 were taken from PDB ID: 5E6J[49]. For the double mutant setup, the mutations S67V and L76T were introduced using MODELLER[50]. For SCoV2-PLpro with bound K48-Ub_2, we set up two models. We combined the substrate coordinates taken from PDB ID: 5E6J with (1) the X-ray crystal structure of the unbound form (PDB ID: 6W9C, re-refined by T. Croll (University of Cambridge, UK) (https://drive.google.com/drive/folders/1JBo50CdkBU7K1pFThuqrzhQ-NcsIAWyG) and (2) with the X-ray crystal structure of the SCoV2-PLpro–mouse ISG15 complex (PDB ID: 6YVA) after PLpro alignment using PyMol[51]. In all di-ubiquitin systems, the triazole linker was replaced with Lys using MODELLER. To mimic the linker, a harmonic-distance restraint potential was applied between the backbone carbonyl carbon atoms of Lys48 and Gly75 with a target distance of 9.5 Å and a force constant of 502,080 kJ mol^{-1} nm^{-2}. The covalent propargylamide linker was removed.

SCoV-PLpro and SCoV2-PLpro in complex with inhibitor GRL-0617—The coordinates of the SCoV-PLpro–GRL-0617 complex were taken from PDB ID: 3E9S[18]. The oxidized Cys112 was changed to the reduced form (SH) using MODELLER. The simulation model of the SCoV2-PLpro– GRL-0617 complex was built according to the X-ray structure of the unbound form of SCoV2-PLpro (PDB ID: 6W9C, re-refined by T. Croll). The coordinates of the compound GRL-0617 were modelled according to PDB ID: 3E9S after PLpro alignment using PyMol. The blocking loop 2 (BL2 loop, GNYQCGH) capping the GRL-0617 binding site was remodelled according to the SCoV-PLpro X-ray crystal structure of the complex (PDB ID: 3E9S)[18] using MODELLER. The GRL-0617 ligand was parameterized with the general amber force field (GAFF)[52].

SCoV2-PLpro with mouse ISG15—The X-ray crystal structure of the SCoV2-PLpro–mouse ISG15 complex (PDB ID: 6YVA) served as starting point. Missing residues of SCoV2-PLpro and one Zn ion were modelled according to the X-ray crystal structure (PDB ID: 6W9C, re-refined by T. Croll).

Missing side chains in all setups were modelled using MODELLER. All crystallographic water molecules and ions were retained, except a nickel ion in PDB ID: 5E6J. According to pK_a calculations using PropK_a and additional visual inspections, in all setups His17 of SCoV2-PLpro (His18 of SCoV-PLpro) and His272 of SCoV2-PLpro (His273 of SCoV-PLpro) were charged. We cannot exclude that the protonation state of the catalytic His272 of SCoV2-PLpro (His273 of SCoV-PLpro) is in equilibrium between charged and neutral forms. All other residues were simulated in their physiological protonation state. The proteins were solvated in TIP4P-D water[53] with 150 mM NaCl. Molecular dynamics simulations were carried out using Gromacs 2018[54] and the AMBER99SB*-ILDN-q force field[55–58]. Each system was energy minimized, followed by five equilibration steps, in which we gradually weakened the position restraints on heavy atoms, first in an NVT

ensemble (0.25 ns) and then in an NPT ensemble (4 × 0.5 ns) using a Berendsen thermostat and barostat[59]. Production simulations were run at a temperature of 310 K and a pressure of 1 bar in an NPT ensemble using a Nosé–Hoover thermostat[60,61] and a Parrinello-Rahman barostat[62]. We set up three independent runs of the SCoV2-PLpro systems with bound substrates, starting from different MODELLER results for the apo-like model of SCoV2-PLpro:K48-Ub_2 and for the SCoV2-PLpro–mouse ISG15 complex. For simulations with bound substrates and with bound inhibitor, we monitored the root-mean-square deviation (r.m.s.d.) of each backbone substrate (distal ubiquitin in K48-Ub_2 and N-terminal domain of mouse ISG15) and of GRL-0617 (heavy atoms) to the respective equilibrated structure after alignment on the helix backbone of PLpro (without the flexible UBL domain). From simulations of SCoV-PLpro–K48-Ub_2, we extracted the minimum heavy-atom distance between F70 of SARS and I44 of ubiquitin.

Inhibitor IC_{50} determination

For IC_{50} value for inhibitors, ubiquitin–AMC or ISG15–AMC was used as substrate of PLpro and the release of AMC was measured by increase of fluorescence (excitation/emission, 360/487 nm) on a 384-well microplate reader (PHERAstar FSX, BMG Labtech). Five microlitres of solution containing different concentrations of GRL-0617 (200–0 μM) and 10 μM of ubiquitin–AMC or ISG15–AMC were aliquoted into 384 well plate and reaction was initiated by addition of 5 μl of PLpro (30 nM) to the well. Initial velocities of AMC release were normalized against DMSO control. The IC_{50} value was calculated by the dose–response–inhibition function in Graphpad Prism with [inhibitor] vs normalized response equation. The experiment was repeated three times.

Mass-spectrometry

For interactome analysis, A549 cells were transfected with wild-type or mutant (C111S) SCoV-PLpro or SCoV2-PLpro, and for comparison between SARS-CoV and SARS-CoV-2, PLpro(C111S) versions of both proteins were transfected. Cells were stimulated with IFN-α (200 U ml^{-1}) for 36 h to mimic an infection scenario. Cells were lysed in ice cold lysis buffer (50 mM Tris-Cl, pH 7.5; 150 mM NaCl; 1% Triton X-100) and equal amounts of lysates were incubated with GFP nanotrap beads in IP buffer (Lysis buffer without detergent). After incubation, immunoprecipitates were washed three times with wash buffer (50 mM Tris-HCl, pH7.5; 400 mM NaCl; 0.5 mM EDTA) and two times with IP buffer. Then, beads were incubated with 25 μl of 50 mM Tris-HCl (pH 8.5) containing 4 M urea, 1 mM TCEP, 4 mM chloroacetamide for 1 h in the dark at 37 °C. Afterwards, samples were diluted with 50 mM Tris-HCl pH 8.5 to a final urea concentration <2 M and digested with 0.5 μg trypsin (Promega) at 37 °C overnight. Digests were acidified using trifluoroacetic acid to a pH of 2–3 and peptides were desalted using C18-stage tips[63]. Peptides were labelled with tandem mass tag (TMT) reagents (Thermo fisher) as described previously[64]. In brief, peptides were resuspended in TMT labelling buffer (0.2 M EPPS pH 8.2, 20% acetonitrile) and were mixed with TMT reagents in a 2:1 TMT: peptide ratio. Reaction was performed for one hour at room temperature and subsequently quenched by addition of hydroxylamine to a final concentration of 0.5% at room temperature for 15 min. Samples were pooled in equimolar ratio, acidified and again cleaned-up using C18-stage tips. After drying, peptides were resuspended in 0.1% formic acid for liquid chromatography–mass spectrometry. All mass

spectrometry data was acquired in centroid mode on an Orbitrap Fusion Lumos mass spectrometer hyphenated to an easy-nLC 1200 nano HPLC system with a nanoFlex ion source (ThermoFisher Scientific). A spray voltage of 2.6 kV was applied with the transfer tube heated to 300 °C and funnel RF set to 30%. Internal mass calibration was enabled (lock mass 445.12003 *m*/*z*). Peptides were separated on a self-made 32 cm long, 75 µm internal diameter fused-silica column, packed in house with 1.9 µm C18 particles (ReproSil-Pur, Dr. Maisch) and heated to 50 °C using an integrated column oven (Sonation). HPLC solvents consisted of 0.1% formic acid in water (buffer A) and 0.1% formic acid, 80% acetonitrile in water (buffer B). Peptides were eluted by a nonlinear gradient from 7 to 40% buffer B over 90 min followed by a step-wise increase to 95% buffer B in 6 min which was held for another 9 min. Full scan mass spectra (350–1400 *m*/*z*) were acquired with a resolution of 120,000 at *m*/*z* 200, maximum injection time of 100 ms and AGC target value of 4×10^5. The 20 most intense precursors per full scan with a charge state between 2 and 5 were selected for fragmentation ('Top 20'), isolated with a quadrupole isolation window of 0.7 Th and fragmented via higher-energy collisional dissociation applying a normalized collision energy of 38%. MS2 scans were performed in the Orbitrap using a resolution of 50,000 at *m*/*z* 200, maximum injection time of 86 ms and automatic gain control target value of 1×10^5. Repeated sequencing of already acquired precursors was limited by setting a dynamic exclusion of 60 s and 7 ppm and advanced peak determination was deactivated. Raw mass spectrometry data were analysed with Proteome Discoverer (v.2.4, ThermoFisher Scientific) using Sequest HT as a search engine and performing re-calibration of precursor masses by the Spectrum RC-node. Fragment spectra were searched against the human reference proteome ('one sequence per gene', 20,531 sequences, version March 2020) and protein sequences for SARS (15 sequences, version March 2020) and CoV2 (14 sequences, version February 2020) downloaded from Uniprot in March 2020, as well as common contaminants as included in 'contaminants.fasta' provided with the MaxQuant software. Static modifications were TMT at the peptide N terminus and lysines as well as carbamidomethyl at cysteine residues, dynamic modifications were set as oxidation of methionine and acetylation at the protein N-terminus. Matched spectra were filtered with Percolator, applying a false discovery rate of 1% on peptide spectrum match and protein level. Reporter intensities were normalized to the total protein intensities in Proteome Discoverer, assuming equal sample loading and additionally by median normalization using the NormalyzerDE package[65]. Statistically significant changes between samples were determined in Perseus (v.1.6.6.0) and significant candidates were chosen having *p*-value ≤0.01 and $\log_2$(fold change) value minimum of ±0.5 (ref. [66]).

Cell culture

Human CaCo-2 cells were obtained from the Deutsche Sammlung vonMikroorganismen und Zellkulturen. Cells were grown at 37 °C in Minimal Essential Medium (MEM) supplemented with 10% fetal bovine serum (FBS) and containing 100 IU ml^{-1} penicillin and 100 µg ml^{-1} streptomycin. A549 and HeLa cells were obtained from ATCC (ATCC CCL-185 and ATCC CCL-2, respectively). All cell lines used tested negative for mycoplasma.

Antibodies

We used the following antibodies and dilutions for this study: ubiquitin (catalogue (cat.) no. 3936S, Cell Signaling Technology; 1:20:00), ISG15 (cat. no. HPA004627, Sigma Aldrich/Merck; 1:1,000), GAPDH (cat. no. 2118, Cell Signaling Technology; 1:2,000), GFP trap beads (cat no. gta-100, ChromoTek), GFP (cat. no. sc-9996, Santa Cruz Biotechnology; 1:2,000), IRF3 (cat. no. 4302, Cell Signaling Technology; 1:2,000), phospho-IRF3(Ser396) (cat. no. 4947, Cell Signaling Technology; 1:1,000), IκBα (cat. no. 4812, Cell Signaling Technology; 1:2,000), phospho-IκBα(Ser32/36) (cat. no. 9246, Cell Signaling Technology; 1:1,000), TBK1 (cat. no. 3013, Cell Signaling Technology; 1:2,000), pTBK1 (cat. no. 3300-1 Epitomics; 1:1,000), NF-κB p65 (cat. no. 8008, Santa Cruz Biotechnology; 1:2,000), lamin B1 (cat. no. sc-373918, Santa Cruz Biotechnology; 1:2,000).

Virus preparation

SARS-CoV-2 strain FFM1 (accession no. MT358638)[67] was isolated from travellers returning from Wuhan (China) to Frankfurt (Germany) using CaCo-2 cells. SARS-CoV-2 FFM1 stocks used in the experiments had undergone one passage on CaCo-2 cells, as described previously[25]. Virus titres were determined as $TCID_{50}$ per ml in confluent cells in 96-well microtitre plates.

Antiviral and cytotoxicity assays

Confluent layers of CaCo-2 cells in 96-well plates were infected with SARS-CoV–2 FFM1 at a MOI of 0.01. Virus was added simultaneously with GRL-0617 and incubated in MEM supplemented with 1% FBS with different drug dilutions. CPE was assessed visually 48 h after infection. To assess effects of GRL-0617 on CaCo-2 cell viability, confluent cell layers were treated with different drug concentration. Cell viability was determined by MTT assay, modified after Mosman[68], as previously described[69]. Data for each condition were collected for at least three biological replicates.

Luciferase activity assay

To analyse the induction of IFN-β induced genes, a luciferase reporter assay was used in A549 cells. In brief, an expression construct containing the luciferase ORF and the IFN-β promoter (IFN-β-luciferase) was co-transfected with either a GFP control plasmid or the designated PLpro plasmid. For all transfections, 100 ng of luciferase plasmid, 400 ng of PLpro or GFP vector was used in each well of a 12-well plate All transfections were performed in triplicate and the average of three experiments is shown in figures. Twenty-four hours after transfection, cells were treated with 500 ng poly(I:C) for 18 h or 50 ng ml^{-1} of TNF for 30 min. Luciferase expression was measured using the Luciferase Reporter Assay System (Promega). Fold change was calculated by taking vector treated with poly(I:C) or TNF as 1.

Immunofluorescence and confocal imaging

HeLa cells expressing GFP-tagged PLpro was treated with TNF (50 ng ml^{-1}) for 45 min. Cells were fixed with paraformaldehyde, blocked in 5% serum and immunostained overnight at 4 °C with antibody against p65. Confocal imaging was performed using the Zeiss

LSM780 microscope system. An Ar ion laser (for excitation of GFP at 488 nm), a He-Ne laser (for excitation of Alexa Fluor 546 nm) were used with a 63× 1.4 NA oil-immersion objective. Images were analysed in FIJI to determine colocalization between DAPI and immunostained p65. Results are indicative of 50 cells taken from 3 independent experiments; error bars indicate standard deviation.

Nuclear fractionation

A549 cells from a confluent 60-mm dish were transiently transfected with GFP-tagged PLPro followed by treatment with IFN-α (200 ml^{-1}, 36 h). Cells were lysed in hypotonic buffer (10 mM HEPES (pH 7.4), 2 mM $MgCl_2$, 25 mM KCl, 1 mM DTT, 1 mM PMSF, and protease inhibitor cocktail), kept on ice for 30 min followed by syringe lysis, and 2 M sucrose solution was added dropwise, followed by centrifugation at 1,000*g* for 15 min. The supernatant was saved as the cytosolic fraction. The pellet was washed twice in wash buffer (10 mM HEPES (pH 7.4), 2 mM $MgCl_2$, 25 mM KCl, 250 mM sucrose, 1 mM DTT, 1 mM PMSF, and protease inhibitor cocktail) and saved as the nuclear fraction.

Quantification of viral and cellular RNA

SARS-CoV-2 RNA from cell culture supernatant samples was isolated using ACL buffer and the QIAamp 96 Virus kit (Qiagen) according to the manufacturer's instructions. RNA was subjected to OneStep quantitative PCR with reverse transcription (RT–qPCR) analysis using the LightCycler Multiplex RNA Virus Master kit (Roche). Intracellular RNA was isolated using RLT buffer and the RNeasy 96 HT Kit according to the manufacturer's instructions. PCR was performed on a CFX96 Real-Time System, C1000 Touch Thermal Cycler. Primers and probe were adapted from the WHO protocol[70] targeting the open reading frame of RNA-dependent RNA polymerase (*RdRP*) of both SARS-CoV-2: RdRP_SARSr-F2 (GTGARATGGTCATGTGTGGCGG) and RdRP_SARSr-R1 (CARATGTTAAASACACTATTAGCATA) primers were used at a final concentration of 0.4 μM and RdRP_SARSr_P2 probe (6-Fam CAG-GTGGAACCTCATCAGGAGATGC BBQ1) was used at 0.2 μM. Primers for *ACTB* (fwd: CATCGAGCACGGCATCGTCA; rev: TAGCACAGCCT GGATAGCAAC)[71], *ISG15* (fwd: GAGAGGCAGCGAACTCATCT; rev: AGGGAC ACCTGGAATTCGTT)[72] *IL6* (fwd: GCAGAAAAAGGCAAAGAATC; rev: CTACATTTGCCGAAGAGC), *IL8* (fwd: GTTTTTGAAGAGGGCTGAG; rev: TTTGCTTGAAGTTTCACTGG) and 18S rRNA (fwd: AGAAACGGC TACCACATCCA ; rev: CACCAGACTTGCCCTCCA) were used for SYBR green-based detection of cellular genes in a final concentration of 0.4 μM per reaction. For each condition, three biological replicates were used. Mean and s.d. were calculated for each group. For interferon-responsive genes, the following primers were used. *MX1* (fwd: TTTTCAAGAAGGAGGCCAGCAA; rev: TCAGGAACTTCCGCTTGT CG), *OAS1* (fwd: TGGCCTTCTATGCCCTCTATCC; rev: TCCCATCAGGTGC ACAGAAGA) and *PKR* (fwd: GGAACTTTGCGATACATGAGCC; rev: CGTCCC GTAGGTCAGTGAAAAA). SARS-CoV-2 subgenomic RNA4 encoding E gene, which is processed during discontinuous transcription in productively infected cells[73], was quantified using primer pairs (fwd: AACGTACCTGTCTCTTCCGA; rev: CCAACCAACTTTCGATCTCTTGT) spanning a junction of the SARS-CoV-2 subgenomic RNAs and used as a measure of viral activity.

Extended Data

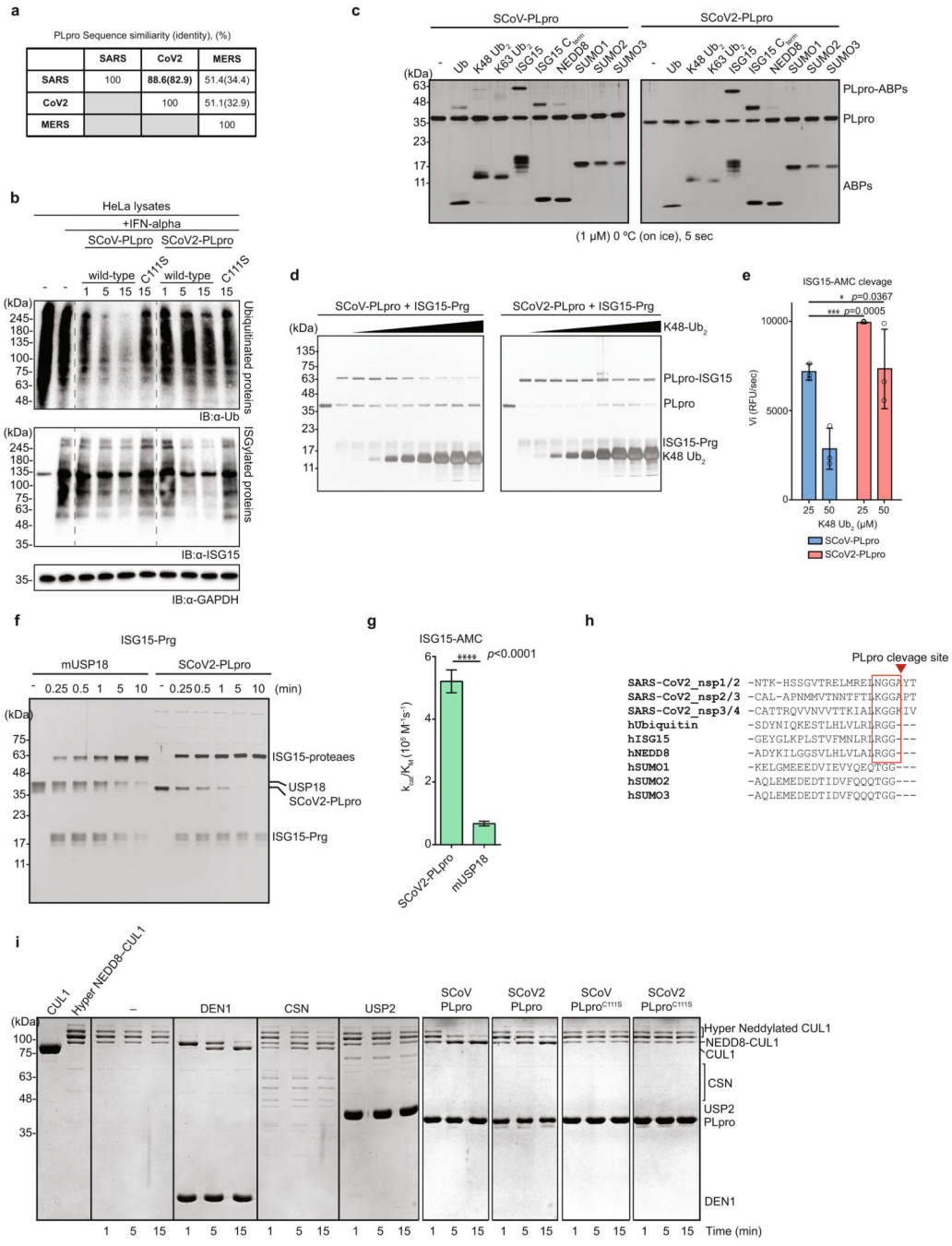

Extended Data Fig. 1. Biochemical properties of SCoV2-PLpro.

a, Sequence similarity of PLpro from SARS, MERS and SARS-CoV-2. **b**, IFN-α-treated HeLa cell lysates were incubated with PLpro for indicated time points and analysed by immunoblot **c**, Propargylamide-activity based probes of ubiquitin like modifiers were reacted with (left) SCoV-PLpro (right) PLpro^{CoV2}. **d**, ISG15-Prg were incubated with SCoV-PLpro (left) or SCoV2-PLpro (right) with increasing amount of non-hydrolysable

$K48\text{-}Ub_2$. **e**, Initial AMC release rate from ISG15-AMC. Purified SCoV-PLpro and SCoV2-PLpro were incubated with ISG15-AMC and indicated amounts of $K48\text{-}Ub_2$. The release of AMC was measured by increase of fluorescence at (Ex./Em. 360/487 nm). **f**, Purified mUSP18 (left) and SCoV2-PLpro (right) were incubated with ISG15-propargylamide activity-based probes for indicated time points. **g**, Catalytic efficiency (k_{cat}/K_m) of mUSP18 and SCoV2-PLpro on ISG15-AMC cleavage. **h**, Sequence alignment of PLpro cleavage site of Nsp1/2, Nsp2/3, Nsp3/4 from SARS-CoV2 and human ubiquitin like modifiers. **i**, Hyper-NEDDylated CUL1-RBX1 was incubated with purified PLpro proteins for indicated time points at 37 °C. Reactions were performed side-by-side by with well-characterized deneddylating enzymes (DEN1 with broad specificity or COP9 Signallosome CSN specific for NEDD8 linked directly to a cullin), or the broad specificity deubiquitinating enzyme USP2 as controls. Data in **e**, **g** are presented as mean ± s.d. ($n = 3$, independent experiments). $^{**}P < 0.01$, $^{***}P < 0.001$, $^{****}P < 0.0001$; two-tailed paired *t*-tests. Experiments in **b–d**, **f**, **i** were repeated three times independently with similar results.

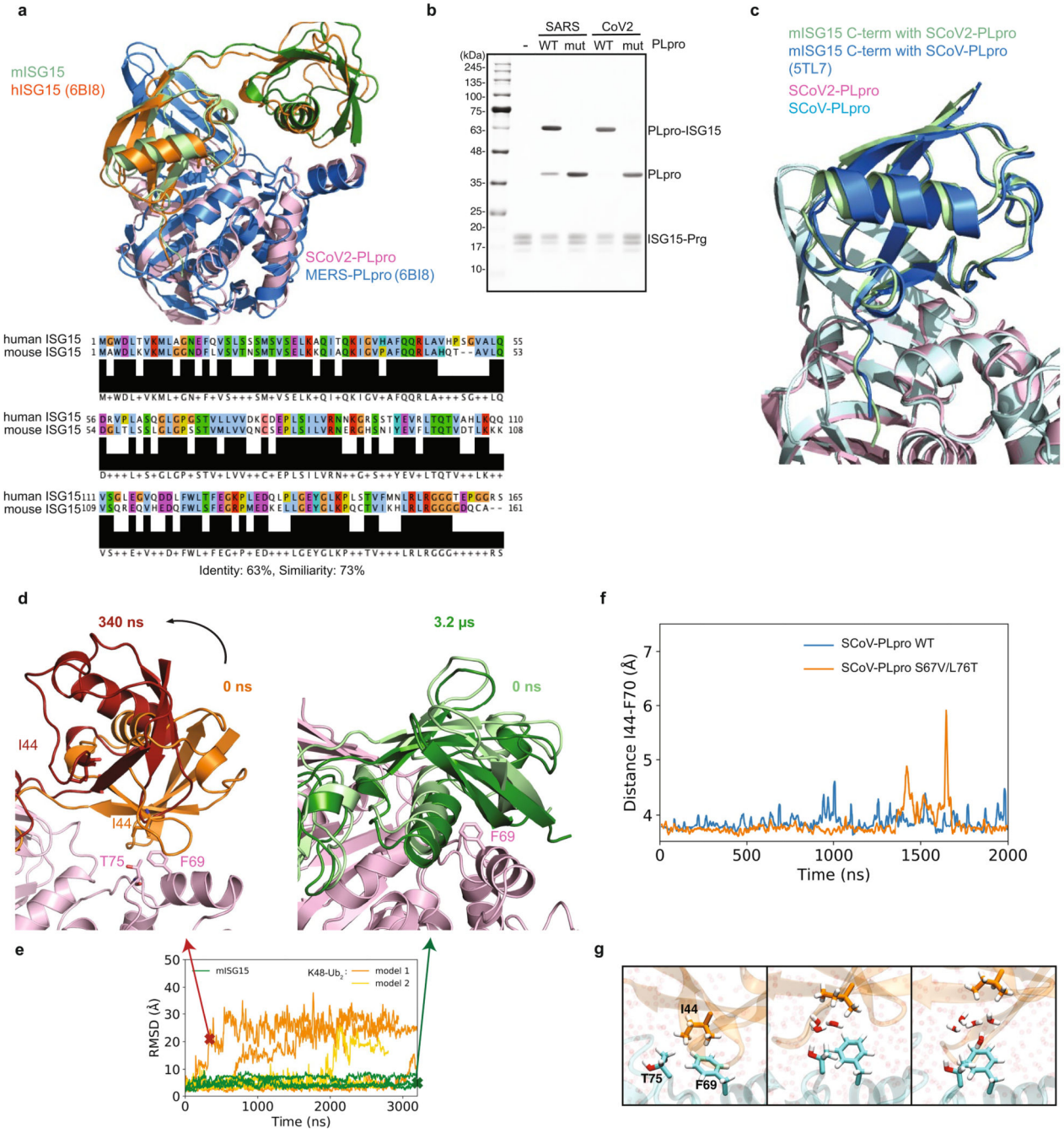

Extended Data Fig. 2. Complex structure of SCoV2-PLpro with mouseISG15.

a, Structural comparison of mouseISG15:SCoV2-PLpro with humanISG15: MERS-PLpro (PDB: 6BI8[16]) and sequence alignment of human and mouse ISG15. **b**, Activity test of wild type or catalytically inactive mutant (C111S) of SCoV-PLpro and SCoV2-PLpro. ISG15 Propargyl-activity based probes were mixed with indicated PLpro proteins. Experiments were repeated three times independently with similar results. **c**, Structural comparison of C-terminal domain of ISG15 in complex with SCoV2-PLpro and SCoV-PLpro (PDB: 5TL7[17]). **d**, Snapshots from molecular dynamics simulations of SCoV2-PLpro (light pink cartoon)

with (left) K48-Ub_2 at 340 ns and (right) mISG15 at 3.2 μs. Key residues in the interface are highlighted. **e**, Backbone r.m.s.d. of the N-terminal domain of mISG15 (green) and of the distal ubiquitin in K48-Ub_2 in an apo-like model (orange, model 1, SCoV2-PLpro coordinates from substrate unbound form, PDB: 6W9C) and in an mISG15-like model (yellow, model 2, SCoV2-PLpro coordinates from substrate bound form, PDB: 6YVA) from their respective SCoV2-PLpro-bound starting structures as function of time. The r.m.s.d. was calculated after superimposing the helix backbone atoms of SCoV2-PLpro. Time points for structural snapshots in **e**) are marked with a cross. **f**, Minimum heavy atom distance between F70 (SARS) and I44(Ub) in wild type and double mutant (S67V/L76T) of SCoV-PLpro:K48-Ub_2 as function of time. **g**, Water mediated dissociation pathway. Left, initial hydrophobic interactions between F69(CoV2), T75(CoV2) and I44(Ub). Middle, water wedges in between T75(CoV2) and I44(Ub). Right, water penetration between T75(CoV2)/F69 (CoV2) and I44(Ub) leads to dissociation.

Europe PMC Funders Author Manuscripts

Europe PMC Funders Author Manuscripts

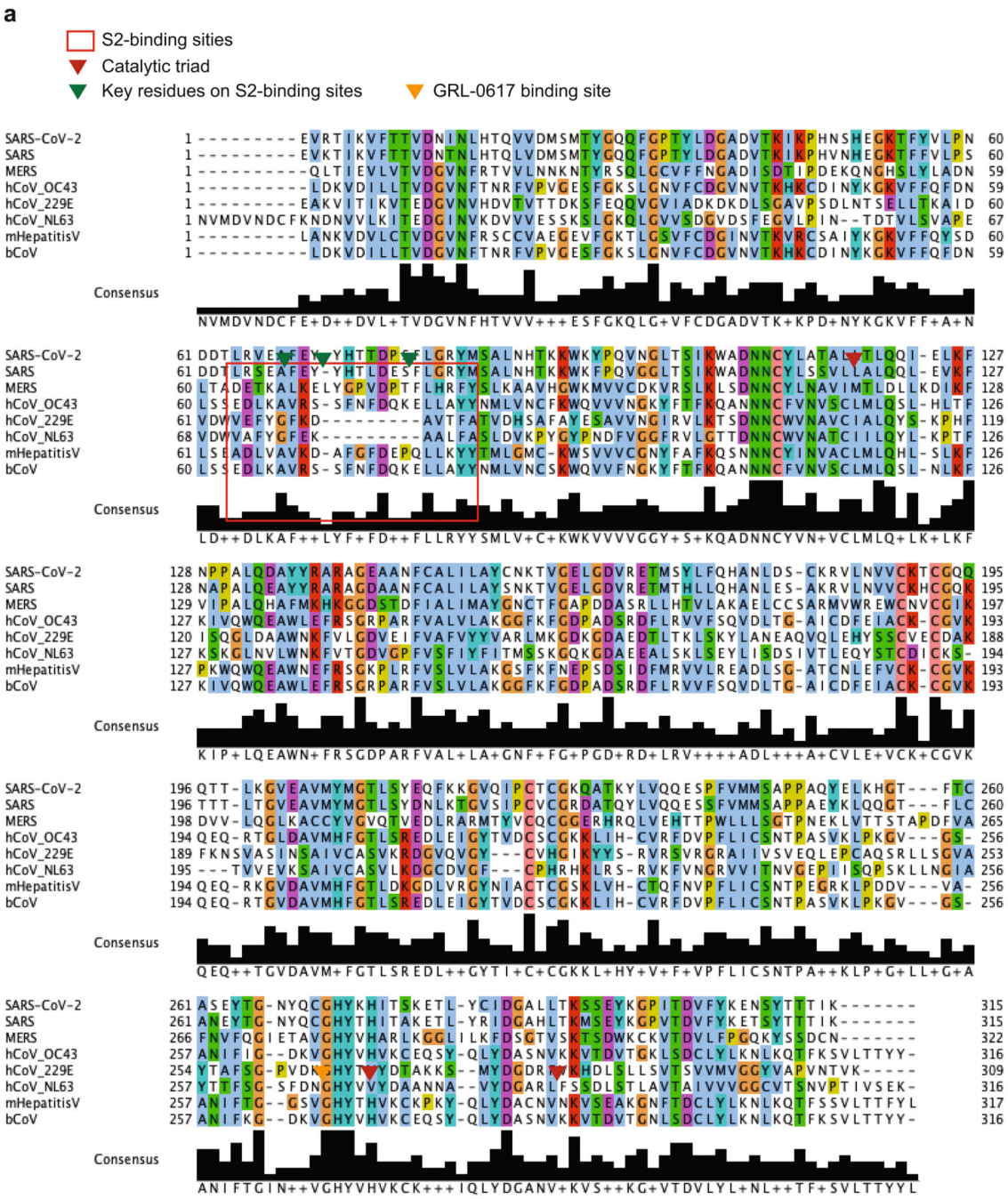

Extended Data Fig. 3. Sequence alignment of papain like protease domain from corona viruses.

The amino acid sequences of papain-like protease domain from eight different coronaviruses (SARS-CoV-2, SARS, MERS, humanCoV-OC43, humanCoV-229E, humanCoV-NL63, murine HepatitisV, bovine CoV) were aligned with Clustal Omega. Accession numbers: SARS-CoV-2 (NC_045512), SARS (PDB: 3MJ5), MERS (PDB: 5W8U), hCoV-OC43 (AY585228), hCoV-229E (X69721), hCoV-NL63 (NC_005831), murine HepatitisV (NC_001846), bCoV (NC_003045).

Europe PMC Funders Author Manuscripts

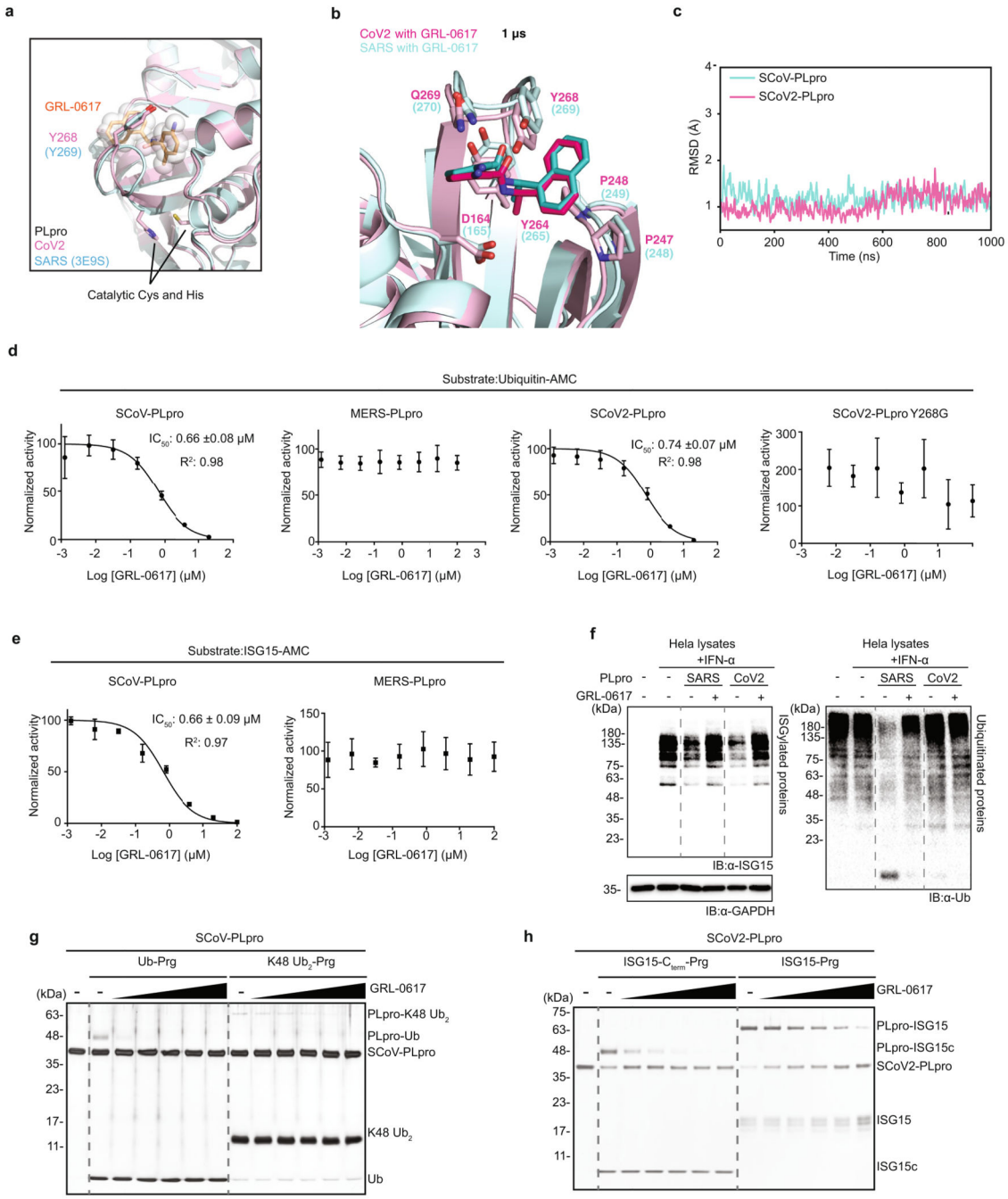

Extended Data Fig. 4. Structural analysis of GRL-0167, SCoV2-PLpro complex.

a, Structural model of GRL-0617 bound SCoV2-PLpro. The conformation of Tyr268 on SCoV2-PLpro and the coordinates of GRL-0617 is obtained from the SCoV-PLpro:GRL-0617 structure (PDB: 3E9S[18]) **b**, Snapshots of SCoV-PLpro (light cyan) and SCoV2-PLpro (light pink) with bound GRL-0617 (dark colours) after 1 μs of molecular dynamics simulation. The protein backbones are shown in cartoon representation, and the ligand with contacting residues as sticks. **c**, r.m.s.d. of the GRL-0617 bound to SCoV-PLpro (light blue) and SCoV2-PLpro (light pink) as a function of time. The r.m.s.d. was calculated

for non-hydrogen atoms of GRL-0617 with respect to the starting structures in the MD simulations after superimposing the helix backbone atoms of PLpro. **d**, In vitro PLpro inhibition assay. Initial velocity of AMC release from ubiquitin-AMC in different concentration of GRL-0617 was measured and normalized to DMSO control. IC_{50} value of GRL-0617 to SCoV-PLpro and SCoV2-PLpro were presented. Data are presented as mean ± s.d. (n = 3, independent experiments). **e**, In vitro PLpro inhibition assay. Initial velocity of AMC release from ISG15-AMC in different concentration of GRL-0617 was measured and normalized to DMSO control. IC_{50} value of GRL-0617 to SCoV-PLpro were presented. Data are presented as mean ± s.d. (n = 3, independent experiments). **f**, Effects of GRL-0617 on (left) deISGylase or (right) deubiquitinase activity of PLpro of SARS and SARS-CoV-2. **g**, Effects of GRL-0617 on SCoV-PLpro activity to (left) ubiquitin or (right) K48-Ub_2 propargyl activity-based probes. Inhibitory effect of GRL-0617 on ubiquitin species was tested with various concentration of GRL-0617 (0-400 μM). **h**, Effects of GRL-0617 on SCoV2-PLpro activity to (left) ISG15-C_{term} or (right) ISG15 propargylamide activity-based probes. Inhibitory effect of GRL-0617 on ISG15 was tested with various concentration of GRL-0617 (0-400 μM). Experiments in **f**–**h** were repeated three times independently with similar results.

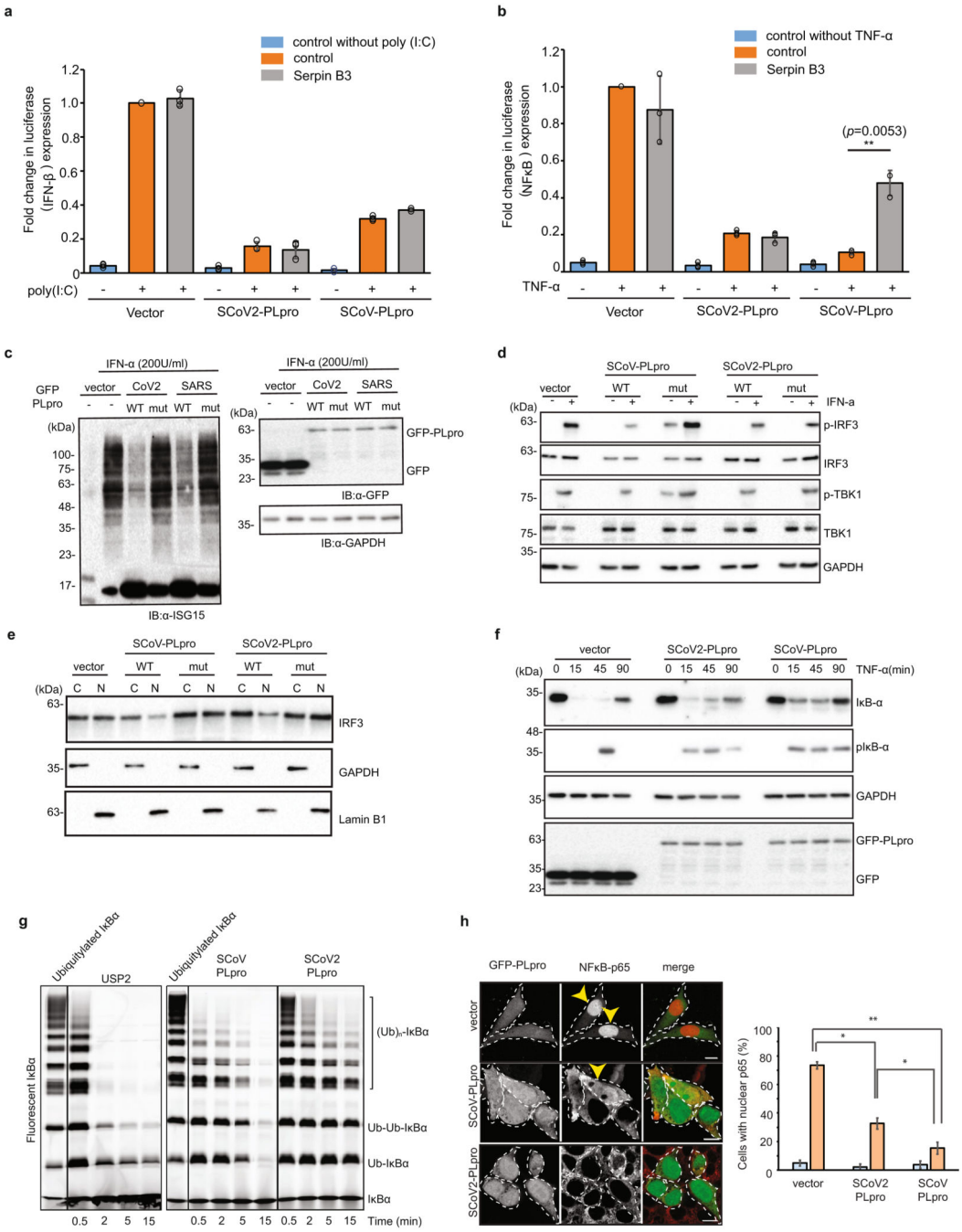

Extended Data Fig. 5. Physiological roles of PLpro in cells.

a, **b**, Effect of SERPIN B3 on PLpro mediated IFN-β (**a**) or NF-κB p65 (**b**) expression level. A549 Cells were co-transfected with indicated GFP-PLpro and Myc-SERPINs and treated with either poly(I:C) or TNF-α to induce IFN-β and NF-κB p65 expression, respectively. Fold changes of luciferase level are presented. **c**, Effect of PLpro on IFN-induced cellular ISGylation. A549 cells were transfected with indicated PLpro plasmids and treated with IFN-α. Lysates were analysed by immune-blotting with indicated antibodies. **d**, **e**, Effect of PLpro on IFN-signalling pathway. **d**, A549 cells were transfected with indicated PLpro

plasmids and treated with IFN-α. Lysates were analysed by immune-blotting with indicated antibodies. **e**, Effect of PLpro on cellular localization of IRF3. Cells from **d** were fractionated into cytosol and nucleus and the level of IRF3 was analysed. Lamin B1 was used for nuclear fraction control. **f**, Effect of PLpro on the NF-κB pathway. IκB-α phosphorylation and degradation were examined from A549 cells expressing indicated GFP-PLpro under treatment of TNF-α. **g**, in vitro IκBα deubiquitylation assay. Ubiquitinated IκBα were incubated with SCoV-PLpro or SCoV2-PLpro. USP2 were used as positive control. **h**, Effect of PLpro on NF-κB p65 cellular localization. Scale bar, 10 μm. Data in **a**, **b**, **h** are presented as mean ± s.d. ($n = 3$, independent experiments). *$P < 0.05$, **$P < 0.01$; two-tailed paired *t*-tests. Experiments in **c**–**h** were repeated three times independently with similar results. **e**, Effect of PLpro on the NF-κB pathway. IκB-α phosphorylation and degradation were examined from A549 cells expressing indicated GFP-PLpro under treatment of TNF-α.

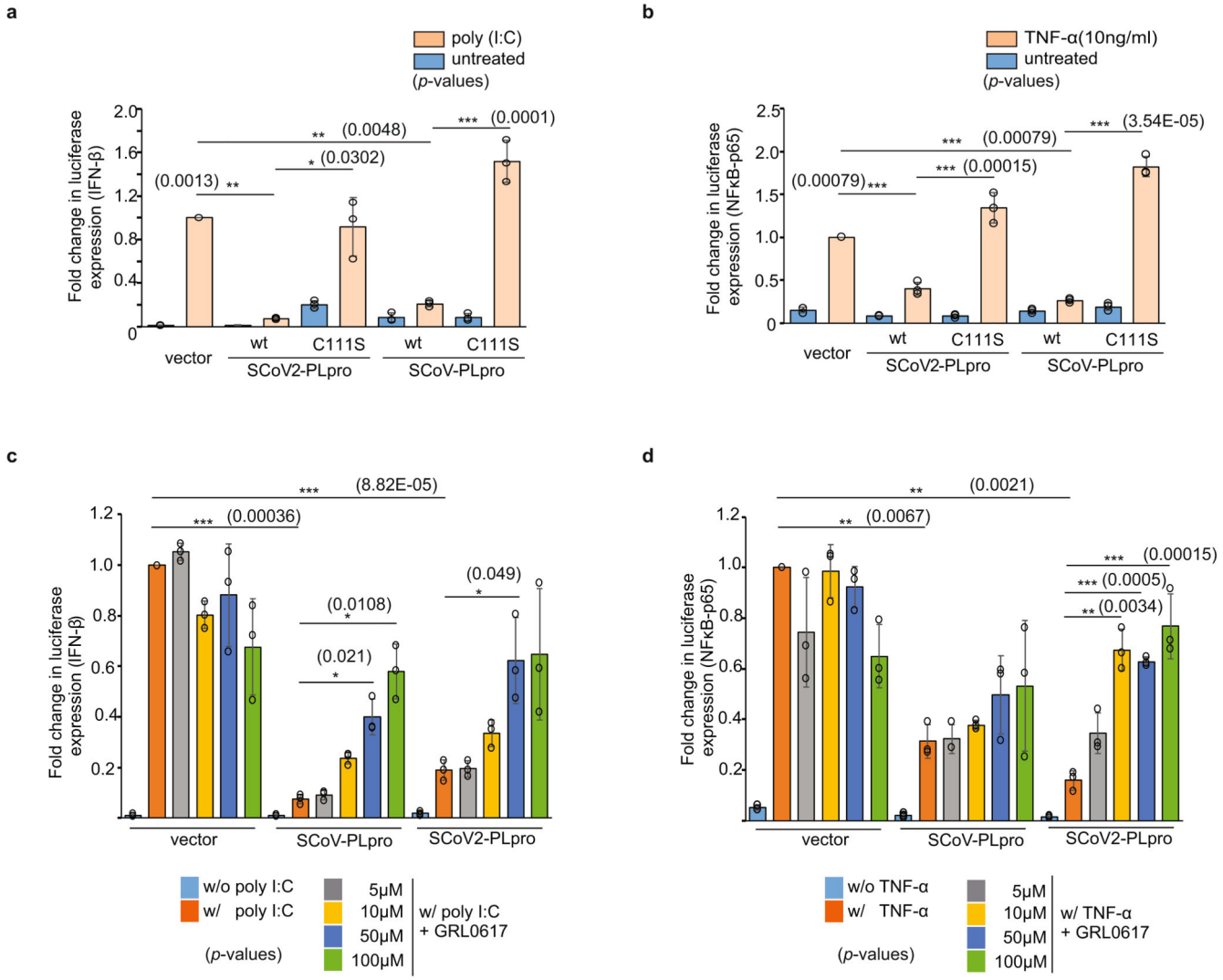

Extended Data Fig. 6. Effect of PLpro on IFN-β or NF-κB p65 expression level.

Europe PMC Funders Author Manuscripts

a, **b**, Effect of PLpro on IFN-β (**a**) or NF-κB p65 (**b**) expression level. A549 Cells were transfected with indicated GFP-PLpro and treated with either poly(I:C) or TNF-α to induce IFN-β and NF-κB p65 expression, respectively. **c**, **d**, Effect of GRL-0617 on PLpro mediated IFN-β (**c**) or NF-κB p65 (**d**) expression level. A549 Cells were transfected with indicated GFP-PLpro and treated with either poly (I:C) or TNF-α to induce IFN-β and NF-κB p65 expression, respectively. GRL-0617 is treated as indicated. All data are presented as mean ± s.d. ($n = 3$, independent experiments). *$P < 0.05$, **$P < 0.01$, ***$P < 0.001$; two-tailed paired t-tests.

Europe PMC Funders Author Manuscripts

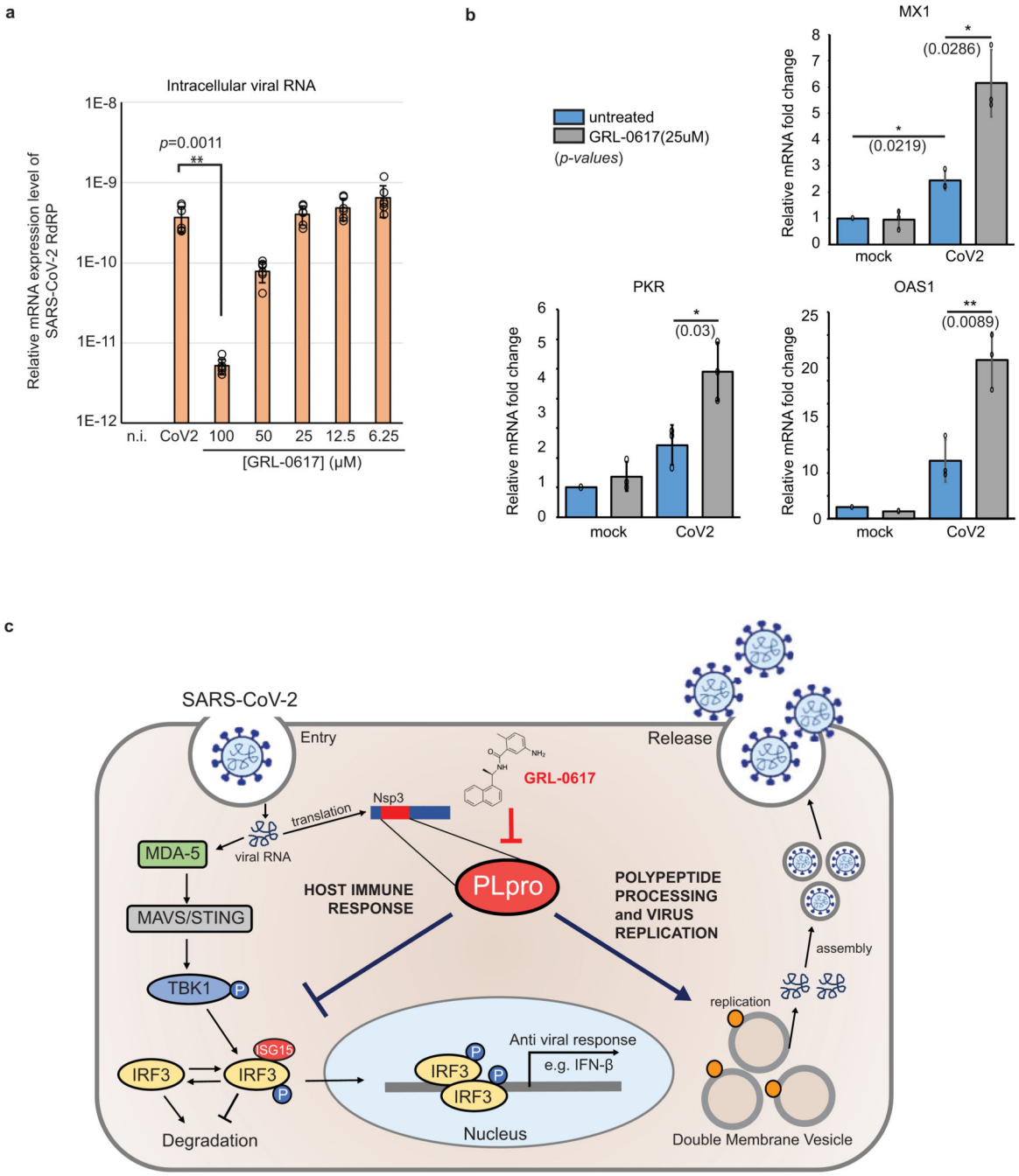

Extended Data Fig. 7. Inhibitory effects of GRL-0617 on SARS-CoV2 infection.

a, Intracellular virus production was analysed by PCR targeting SARS-CoV-2 RdRP mRNA. Relative expression level of SARS-CoV2-2 genomic RNA was normalized to cellular GAPDH level. **b**, Intracellular RNA was isolated from cells without infection or cells infected with SARS-CoV-2 with or without treatment of GRL-0617. Relative mRNA-level fold change of indicated genes were analysed in a qRT–PCR analysis and normalized to ACTB levels. Data in **a**, **b** are presented as mean ± s.d. ($n = 3$, independent experiments). *$P < 0.05$, **$P < 0.01$; two-tailed paired t-tests. **c**, Schematic representation of the role of

Europe PMC Funders Author Manuscripts

SARS-CoV-2 PLpro in the viral life cycle. The physiological role of SCoV2-PLpro in both host-immune response and polypeptide processing is shown. Inhibition of PLpro by GRL-0617 is also presented.

Extended Data Table 1
Data collection and refinement statistics (molecular replacement)

	SCoV2-PLpro (CUIS): mISG15 (PDB: 6YVA)
Data collection	
Space group	P 62 2 2
Cell dimensions	
a, b, c (Å)	157.047, 157.047, 83.633
α, β, γ (°)	90, 90, 120
Resolution (Å)	45.34-3.185 (3.298-3.185)[†]
R_{sym} or R_{merge}	0.05751 (0.5689)
$I/\sigma I$	8.58(1.19)
Completeness (%)	99.61 (97.77)
Redundancy	2.0 (2.0)
Refinement	
Resolution (Â)	45.34-3.185(3.298-3.185)[†]
No. reflections	10590(1008)
R_{work} / R_{free}	0.2496 /0.2902
No. atoms	3407
Protein	3383
Ligand/ion	1
Water	23
B-factors	87.60
Protein	87.72
Ligand/ion	167.02
Water	66.67
R.m.s. deviations	
Bond lengths (Å)	0.004
Bond angles (°)	0.65

Statistics for data collection and refinement are presented.

[*] A single crystal was used for data collection and structure determination.

[†] Values in parentheses are for highest-resolution shell.

Extended Data Table 2
Kinetic parameters on AMC substrates

	Kinetic Parameter	Triazole-linked K48-Ub_2-AMC	ISG15-AMC
SARS-CoV-2			
	Apparent k_{cat}/K_M [$M^{-1}s^{-1}$]	2.41 ± 0.94 (E+05)	5.21 ±0.36 (E+05)
PLpro			

Europe PMC Funders Author Manuscripts

	Kinetic Parameter	Triazole-linked K48-Ub_2-AMC	ISG15-AMC
	$k_{cat}[S^{-1}]$	14.75 ±3.28	4.43 ±0.13
	K_M [μM]	61.23 ±19.76	8.50 ±0.54
	Michaelis-Menten curve fit (R^2)	0.9914	0.9987
SARS			
	Apparent k_{cat}/K_M [$M^{-1}s^{-1}$]	13.94 ±3.50 (E+05)	5.31 ±0.56 (E+05)
PLpro			
	$k_{cat}[S^{-1}]$	62.9 ± 8.45	11.89 + 0.75
	K_M [μM]	45.13 ±9.57	22.41 ±1.89
	Michaelis-Menten curve fit (R^2)	0.9911	0.9997
mUSP18	Apparent k_{cat}/K_M [$M^{-1}s^{-1}$]		0.68 ± 0.07 (E+05)
	$k_{cat}[S^{-1}]$	N.D.	0.06 ± 0.002
	K_M [μM]		0.89 ± 0.093
	Michaelis-Menten curve fit (R^2)		0.9895

Kinetic parameters for SCoV-PLpro, SCoV2-PLpro and murineUSP18 to triazole-linked K48-Ub2-AMC or ISG15-AMC are presented. Values are presented as mean ± s.d. (n = 3, independent experiments).

Extended Data Table 3
Binding kinetics of PLpro to K48-Ub_2 or ISG15

		k_{on} ± S.E.M[a] ($10^2M^{-1}s^{-1}$)	k_{off} S.E.M[a] (10^{-1} s^{-1})	k_d ± S.E.M[a] (μM)	R^2[b]
CoV2 PLpro	Triazole linked K48-Ub_2	158 ±8.00	4.30 ±0.11	27.28 ±1.55	0.99
	HumanISG15	1530 ±52.4	2.15 ±0.06	1.41 ±0.06	0.99
	MouseISG15	122 ±4.48	0.20 ± 0.02	1.64 ±0.17	0.97
SARS PLpro	Triazole linked K48-Ub_2	820 ±32.1	0.81 ±0.02	0.99 ± 0.04	0.98
	HumanISG15	88.8 ±14.5	0.76 ± 0.06	8.60 ±1.56	0.98
	MouseISG15	24.7 ± 0.75	0.23 ± 0.01	9.34 ±0.41	0.98

Binding kinetic parameters for SCoV-PLpro, SCoV2-PLpro to triazole-linked K48-Ub2, humanISG15 or mouseISG15 are presented. Values are presented as mean ± s.e.m. (n = 3, independent experiments).

[a] s.e.m.

[b] R^2, goodness of the curve fit between experimental data and mathematical 1:1 binding curve

Supplementary Material

Refer to Web version on PubMed Central for supplementary material.

Acknowledgements

We thank A. Gubas, C. Joazeiro, D. Hoeller and K. Koch for critical comments on the manuscript. We also thank Swiss Light Source (SLS) for providing special beam time for this project during the peak of the COVID-19 pandemic in Switzerland and W. Meitian and O. Vincent for providing on-site support during the data collection. We thank the Quantitative Proteomics Unit (IBCII, Goethe University Frankfurt) for support and expertise in sample preparation, LC–MS instrumentation and data analysis. This work was supported by the DFG-funded Collaborative Research Centre on Selective Autophagy (SFB 1177), by the Max Planck Society, by NWO (H.O. and G.J.v.d.H.v.N.) by the European Research Council (ERC) under the European Union's Horizon 2020 research and innovation programme (grant agreement no. 789016) to B.A.S., LYSFOR2625 (DFG) to A.B. and (grant agreement no. 742720) to I.D., by the grants from Else Kroener Fresenius Stiftung, Dr. Rolf M. Schwiete Stiftung, and by internal IBC2 funds to I.D.

Data availability

The atomic coordinates of PLpro–mouse ISG15 have been deposited in the PDB with accession code 6YVA. The mass spectrometry data have been deposited to the ProteomeXchange Consortium[74] via the PRIDE partner repository[75] with the data set identifier PXD018983. The papain-like protease domain sequence was obtained from the SARS-CoV-2 complete genome (NCBI nucleotide, severe acute respiratory syndrome coronavirus 2 isolate Wuhan-Hu-1, complete genome; NC_045512). Protein sequence for SCoV2-PLpro Ubl domain (amino acids, 746–1060) of Nsp3 protein from SARS-CoV-2 (Nsp3; YP_009725299.1). Full gel images are shown in Supplementary Fig. 1. Any other relevant data are available from the corresponding authors upon reasonable request. Source data are provided with this paper.

References

1. Harcourt BH, et al. Identification of severe acute respiratory syndrome coronavirus replicase products and characterization of papain-like protease activity. J Virol. 2004; 78:13600–13612. [PubMed: 15564471]
2. Lim KP, Ng LFP, Liu DX. Identification of a novel cleavage activity of the first papain-like proteinase domain encoded by open reading frame 1a of the coronavirus Avian infectious bronchitis virus and characterization of the cleavage products. J Virol. 2000; 74:1674–1685. [PubMed: 10644337]
3. Frieman M, Ratia K, Johnston RE, Mesecar AD, Baric RS. Severe acute respiratory syndrome coronavirus papain-like protease ubiquitin-like domain and catalytic domain regulate antagonism of IRF3 and NF-κB signaling. J Virol. 2009; 83:6689–6705. [PubMed: 19369340]
4. Devaraj SG, et al. Regulation of IRF-3-dependent innate immunity by the papain-like protease domain of the severe acute respiratory syndrome coronavirus. J Biol Chem. 2007; 282:32208–32221. [PubMed: 17761676]
5. Bailey-Elkin BA, et al. Crystal structure of the Middle East respiratory syndrome coronavirus (MERS-CoV) papain-like protease bound to ubiquitin facilitates targeted disruption of deubiquitinating activity to demonstrate its role in innate immune suppression. J Biol Chem. 2014; 289:34667–34682. [PubMed: 25320088]
6. Huang C, et al. Clinical features of patients infected with 2019 novel coronavirus in Wuhan, China. Lancet. 2020; 395:497–506. [PubMed: 31986264]
7. Lu R, et al. Genomic characterisation and epidemiology of 2019 novel coronavirus: implications for virus origins and receptor binding. Lancet. 2020; 395:565–574. [PubMed: 32007145]
8. Zhou P, et al. A pneumonia outbreak associated with a new coronavirus of probable bat origin. Nature. 2020; 579:270–273. [PubMed: 32015507]
9. Sommer S, Weikart ND, Linne U, Mootz HD. Covalent inhibition of SUMO and ubiquitin-specific cysteine proteases by an in situ thiol-alkyne addition. Bioorg Med Chem. 2013; 21:2511–2517. [PubMed: 23535560]
10. Ekkebus R, et al. On terminal alkynes that can react with active-site cysteine nucleophiles in proteases. J Am Chem Soc. 2013; 135:2867–2870. [PubMed: 23387960]
11. Flierman D, et al. Non-hydrolyzable diubiquitin probes reveal linkage-specific reactivity of deubiquitylating enzymes mediated by S2 pockets. Cell Chem Biol. 2016; 23:472–482. [PubMed: 27066941]
12. Basters A, et al. Structural basis of the specificity of USP18 toward ISG15. Nat Struct Mol Biol. 2017; 24:270–278. [PubMed: 28165509]
13. Geurink PP, et al. Profiling DUBs and Ubl-specific proteases with activity-based probes. Methods Enzymol. 2019; 618:357–387. [PubMed: 30850060]
14. Freitas BT, et al. Characterization and noncovalent inhibition of the deubiquitinase and deISGylase activity of SARS-CoV-2 papain-like protease. ACS Infect Dis. 2020; 6:2009–2109.

15. Basters A, et al. Molecular characterization of ubiquitin-specific protease 18 reveals substrate specificity for interferon-stimulated gene 15. FEBS J. 2014; 281:1918–1928. [PubMed: 24533902]
16. Clasman JR, Everett RK, Srinivasan K, Mesecar AD. Decoupling deISGylating and deubiquitinating activities of the MERS virus papain-like protease. Antiviral Res. 2020; 174
17. Daczkowski CM, et al. Structural insights into the interaction of coronavirus papain-like proteases and interferon-stimulated gene product 15 from different species. J Mol Biol. 2017; 429:1661–1683. [PubMed: 28438633]
18. Ratia K, et al. A noncovalent class of papain-like protease/deubiquitinase inhibitors blocks SARS virus replication. Proc Natl Acad Sci USA. 2008; 105:16119–16124. [PubMed: 18852458]
19. Báez-Santos YM, et al. X-ray structural and biological evaluation of a series of potent and highly selective inhibitors of human coronavirus papain-like proteases. J Med Chem. 2014; 57:2393–2412. [PubMed: 24568342]
20. Ghosh AK, et al. Severe acute respiratory syndrome coronavirus papain-like novel protease inhibitors: design, synthesis, protein-ligand X-ray structure and biological evaluation. J Med Chem. 2010; 53:4968–4979. [PubMed: 20527968]
21. Ghosh AK, et al. Structure-based design, synthesis, and biological evaluation of a series of novel and reversible inhibitors for the severe acute respiratory syndrome-coronavirus papain-like protease. J Med Chem. 2009; 52:5228–5240. [PubMed: 19645480]
22. Kilianski A, Baker SC. Cell-based antiviral screening against coronaviruses: developing virus-specific and broad-spectrum inhibitors. Antiviral Res. 2014; 101:105–112. [PubMed: 24269477]
23. Gordon DE, et al. A SARS-CoV-2 protein interaction map reveals targets for drug repurposing. Nature. 2020; 583:459–468. [PubMed: 32353859]
24. Ferguson BJ, Mansur DS, Peters NE, Ren H, Smith GL. DNA-PK is a DNA sensor for IRF-3-dependent innate immunity. eLife. 2012; 1:e00047. [PubMed: 23251783]
25. Bojkova D, et al. Proteomics of SARS-CoV-2-infected host cells reveals therapy targets. Nature. 2020; 583:469–472. [PubMed: 32408336]
26. Ouellet M, et al. Galectin-1 acts as a soluble host factor that promotes HIV-1 infectivity through stabilization of virus attachment to host cells. J Immunol. 2005; 174:4120–4126. [PubMed: 15778371]
27. Schick C, et al. Cross-class inhibition of the cysteine proteinases cathepsins K, L, and S by the serpin squamous cell carcinoma antigen 1: a kinetic analysis. Biochemistry. 1998; 37:5258–5266. [PubMed: 9548757]
28. Takeda A, Yamamoto T, Nakamura Y, Takahashi T, Hibino T. Squamous cell carcinoma antigen is a potent inhibitor of cysteine proteinase cathepsin L. FEBS Lett. 1995; 359:78–80. [PubMed: 7851535]
29. Stetson DB, Medzhitov R. Type I interferons in host defense. Immunity. 2006; 25:373–381. [PubMed: 16979569]
30. Liu T, Zhang L, Joo D, Sun S-C. NF-κB signaling in inflammation. Signal Transduct Target Ther. 2017; 2:17023. [PubMed: 29158945]
31. Sheikh F, Dickensheets H, Gamero AM, Vogel SN, Donnelly RP. An essential role for IFN-β in the induction of IFN-stimulated gene expression by LPS in macrophages. J Leukoc Biol. 2014; 96:591–600. [PubMed: 25024400]
32. Shi H-X, et al. Positive regulation of interferon regulatory factor 3 activation by Herc5 via ISG15 modification. Mol Cell Biol. 2010; 30:2424–2436. [PubMed: 20308324]
33. Blanco-Melo D, et al. Imbalanced host response to SARS-CoV-2 drives development of COVID-19. Cell. 2020; 181:1036–1045. [PubMed: 32416070]
34. Niemeyer D, et al. The papain-like protease determines a virulence trait that varies among members of the SARS-coronavirus species. PLoS Pathog. 2018; 14:e1007296. [PubMed: 30248143]
35. Anson BJ, et al. Broad-spectrum inhibition of coronavirus main and papain-like 2 proteases by HCV drugs. 2020; doi: 10.21203/rs.3.rs-26344/v1
36. Shanker AK, Bhanu D, Alluri A, Gupta S. Whole-genome sequence analysis and homology modelling of the main protease and non-structural protein 3 of SARS-CoV-2 reveal an aza-peptide and a lead inhibitor with possible antiviral properties. New J Chem. 2020; 44:9202–9212.

37. Rut W, et al. Activity profiling and structures of inhibitor-bound SARS-CoV-2-PLpro protease provides a framework for anti-COVID-19 drug design. bioRxiv. 2020; doi: 10.1101/2020.04.29.068890
38. Zhang L, et al. Crystal structure of SARS-CoV-2 main protease provides a basis for design of improved α-ketoamide inhibitors. Science. 2020; 368:409–412. [PubMed: 32198291]
39. Jin Z, et al. Structure of Mpro from COVID-19 virus and discovery of its inhibitors. Nature. 2020; 582:289–293. [PubMed: 32272481]
40. Dai W, et al. Structure-based design of antiviral drug candidates targeting the SARS-CoV-2 main protease. Science. 2020; 368:1331–1335. [PubMed: 32321856]
41. Lo HS, et al. Simeprevir suppresses SARS-CoV-2 replication and synergizes with remdesivir. bioRxiv. 2020; doi: 10.1101/2020.05.26.116020
42. Daczkowski CM, Goodwin OY, Dzimianski JV, Farhat JJ, Pegan SD. Structurally guided removal of DeISGylase biochemical activity from papain-like protease originating from Middle East respiratory syndrome coronavirus. J Virol. 2017; 91:e01067–17. [PubMed: 28931677]
43. Kabsch W. XDS. Acta Crystallogr. D. 2010; 66:125–132. [PubMed: 20124692]
44. McCoy AJ, et al. Phaser crystallographic software. J Appl Cryst. 2007; 40:658–674. [PubMed: 19461840]
45. Afonine PV, et al. Towards automated crystallographic structure refinement with phenix. refine. Acta Crystallogr D. 2012; 68:352–367. [PubMed: 22505256]
46. Emsley P, Lohkamp B, Scott WG, Cowtan K. Features and development of Coot. Acta Crystallogr D. 2010; 66:486–501. [PubMed: 20383002]
47. Baek K, et al. NEDD8 nucleates a multivalent cullin-RING–UBE2D ubiquitin ligation assembly. Nature. 2020; 578:461–466. [PubMed: 32051583]
48. Enchev RI, et al. Structural basis for a reciprocal regulation between SCF and CSN. Cell Rep. 2012; 2:616–627. [PubMed: 22959436]
49. Békés M, et al. Recognition of Lys48-linked di-ubiquitin and deubiquitinating activities of the SARS coronavirus papain-like protease. Mol Cell. 2016; 62:572–585. [PubMed: 27203180]
50. Šali A, Blundell TL. Comparative protein modelling by satisfaction of spatial restraints. J Mol Biol. 1993; 234:779–815. [PubMed: 8254673]
51. Schrödinger L. The PyMol Molecular Graphics System. 2015
52. Wang J, Wolf RM, Caldwell JW, Kollman PA, Case DA. Development and testing of a general amber force field. J Comput Chem. 2004; 25:1157–1174. [PubMed: 15116359]
53. Piana S, Donchev AG, Robustelli P, Shaw DE. Water dispersion interactions strongly influence simulated structural properties of disordered protein states. J Phys Chem B. 2015; 119:5113–5123. [PubMed: 25764013]
54. Abraham MJ, et al. GROMACS: High performance molecular simulations through multi-level parallelism from laptops to supercomputers. SoftwareX. 2015; 1–2:19–25.
55. Hornak V, et al. Comparison of multiple Amber force fields and development of improved protein backbone parameters. Proteins. 2006; 65:712–725. [PubMed: 16981200]
56. Best RB, de Sancho D, Mittal J. Residue-specific α-helix propensities from molecular simulation. Biophys J. 2012; 102:1462–1467. [PubMed: 22455930]
57. Best RB, Hummer G. Optimized molecular dynamics force fields applied to the helix-coil transition of polypeptides. J Phys Chem B. 2009; 113:9004–9015. [PubMed: 19514729]
58. Lindorff-Larsen K, et al. Improved side-chain torsion potentials for the Amber ff99SB protein force field. Proteins. 2010; 78:1950–1958. [PubMed: 20408171]
59. Berendsen HJC, Postma JPM, van Gunsteren WF, DiNola A, Haak JR. Molecular dynamics with coupling to an external bath. J Chem Phys. 1984; 81:3684–3690.
60. Evans DJ, Holian BL. The Nose–Hoover thermostat. J Chem Phys. 1985; 83:4069–4074.
61. Nosé S. A unified formulation of the constant temperature molecular dynamics methods. J Chem Phys. 1984; 81:511–519.
62. Parrinello M, Rahman A. Polymorphic transitions in single crystals: a new molecular dynamics method. J Appl Phys. 1981; 52:7182–7190.

63. Rappsilber J, Ishihama Y, Mann M. Stop and go extraction tips for matrix-assisted laser desorption/ionization, nanoelectrospray, and LC/MS sample pretreatment in proteomics. Anal Chem. 2003; 75:663–670. [PubMed: 12585499]
64. Klann K, Tascher G, Münch C. Functional translatome proteomics reveal converging and dose-dependent regulation by mTORC1 and eIF2α. Mol Cell. 2020; 77:913–925. [PubMed: 31812349]
65. Willforss J, Chawade A, Levander F. NormalyzerDE: online tool for improved normalization of omics expression data and high-sensitivity differential expression analysis. J Proteome Res. 2019; 18:732–740. [PubMed: 30277078]
66. Tyanova S, et al. The Perseus computational platform for comprehensive analysis of (prote)omics data. Nat Methods. 2016; 13:731–740. [PubMed: 27348712]
67. Toptan T, et al. Optimized qRT-PCR approach for the detection of intra- and extracellular SARS-CoV-2 RNAs. Int J Mol Sci. 2020; 21:4396.
68. Mosmann T. Rapid colorimetric assay for cellular growth and survival: application to proliferation and cytotoxicity assays. J Immunol Methods. 1983; 65:55–63. [PubMed: 6606682]
69. Onafuye H, et al. Doxorubicin-loaded human serum albumin nanoparticles overcome transporter-mediated drug resistance in drug-adapted cancer cells. Beilstein J Nanotechnol. 2019; 10:1707–1715. [PubMed: 31501742]
70. Corman VM, et al. Detection of 2019 novel coronavirus (2019-nCoV) by real-time RT-PCR. Euro Surveill. 2020; 25
71. Zhang X, Ding L, Sandford AJ. Selection of reference genes for gene expression studies in human neutrophils by real-time PCR. BMC Mol Biol. 2005; 6:4. [PubMed: 15720708]
72. Moll HP, Maier T, Zommer A, Lavoie T, Brostjan C. The differential activity of interferon-α subtypes is consistent among distinct target genes and cell types. Cytokine. 2011; 53:52–59. [PubMed: 20943413]
73. Kim D, et al. The architecture of SARS-CoV-2 transcriptome. Cell. 2020; 181:914–921. [PubMed: 32330414]
74. Vizcaíno JA, et al. ProteomeXchange provides globally coordinated proteomics data submission and dissemination. Nat Biotechnol. 2014; 32:223–226. [PubMed: 24727771]
75. Vizcaíno JA, et al. 2016 update of the PRIDE database and its related tools. Nucleic Acids Res. 2016; 44(D1):D447–D456. [PubMed: 26527722]

Europe PMC Funders Author Manuscripts

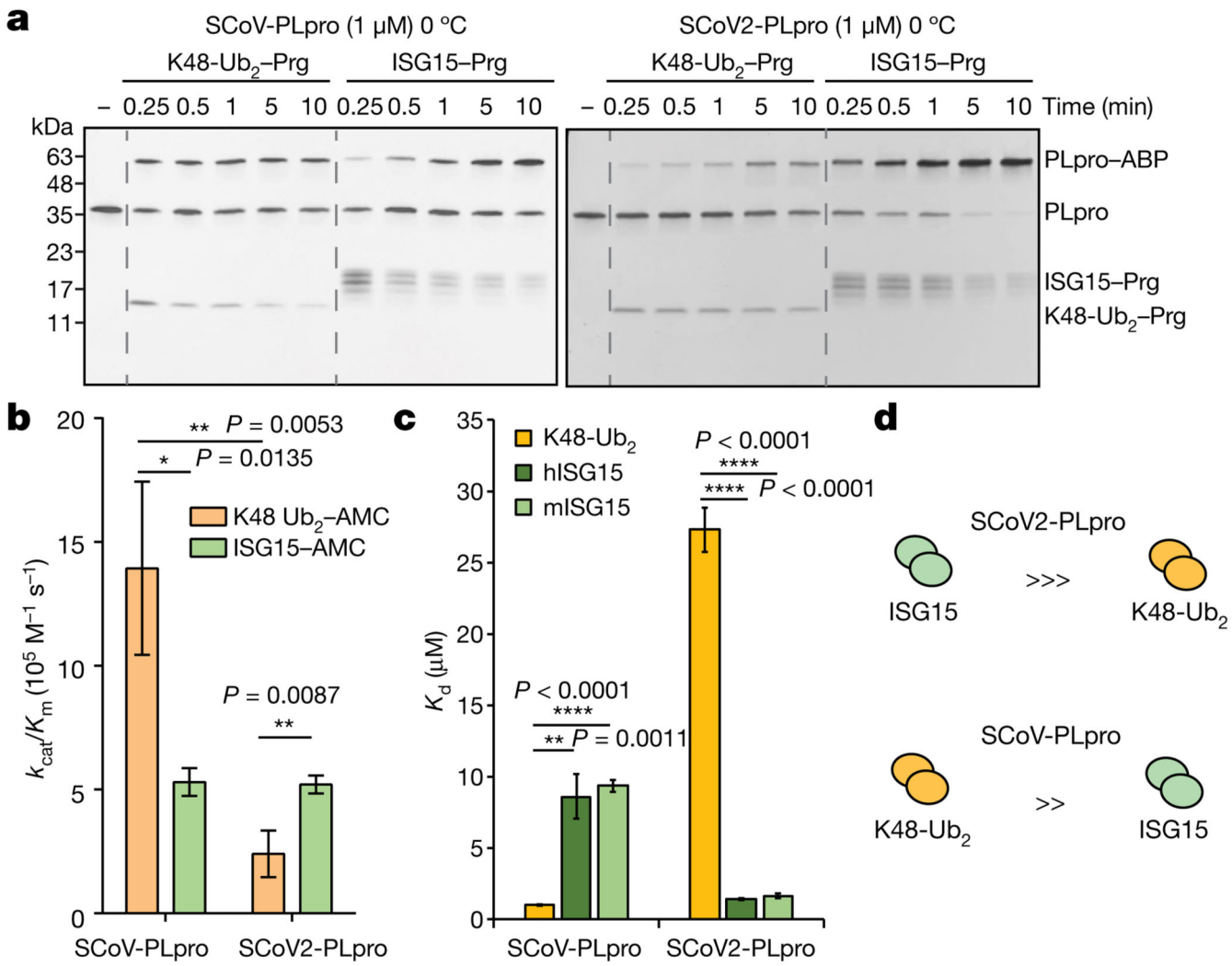

Fig. 1. DeISGylating and deubiquitylating activities of SCoV-PLpro and SCoV2-PLpro.

a, SCoV-PLpro (left) or SCoV2-PLpro (right) were incubated with indicated Prg probes. Experiments were repeated three times independently with similar results. **b**, Catalytic efficiency (k_{cat}/K_m) of SCoV2-PLpro and SCoV-PLpro cleavage of K48-Ub_2-AMC or ISG15-AMC. **c**, Dissociation constant (K_d) of SCoV2-PLpro and SCoV-PLpro. Data in **c**, **d**, are mean ± s.d. or mean ± s.e.m. ($n = 3$ independent experiments). *$P < 0.05$, **$P < 0.01$, ****$P < 0.0001$; two-tailed paired *t*-test. **d**, Schematic representation of substrate specificity of SCoV2-PLpro (red) and SCoV-PLpro (blue). The preferred substrate is shown on the left.

Europe PMC Funders Author Manuscripts

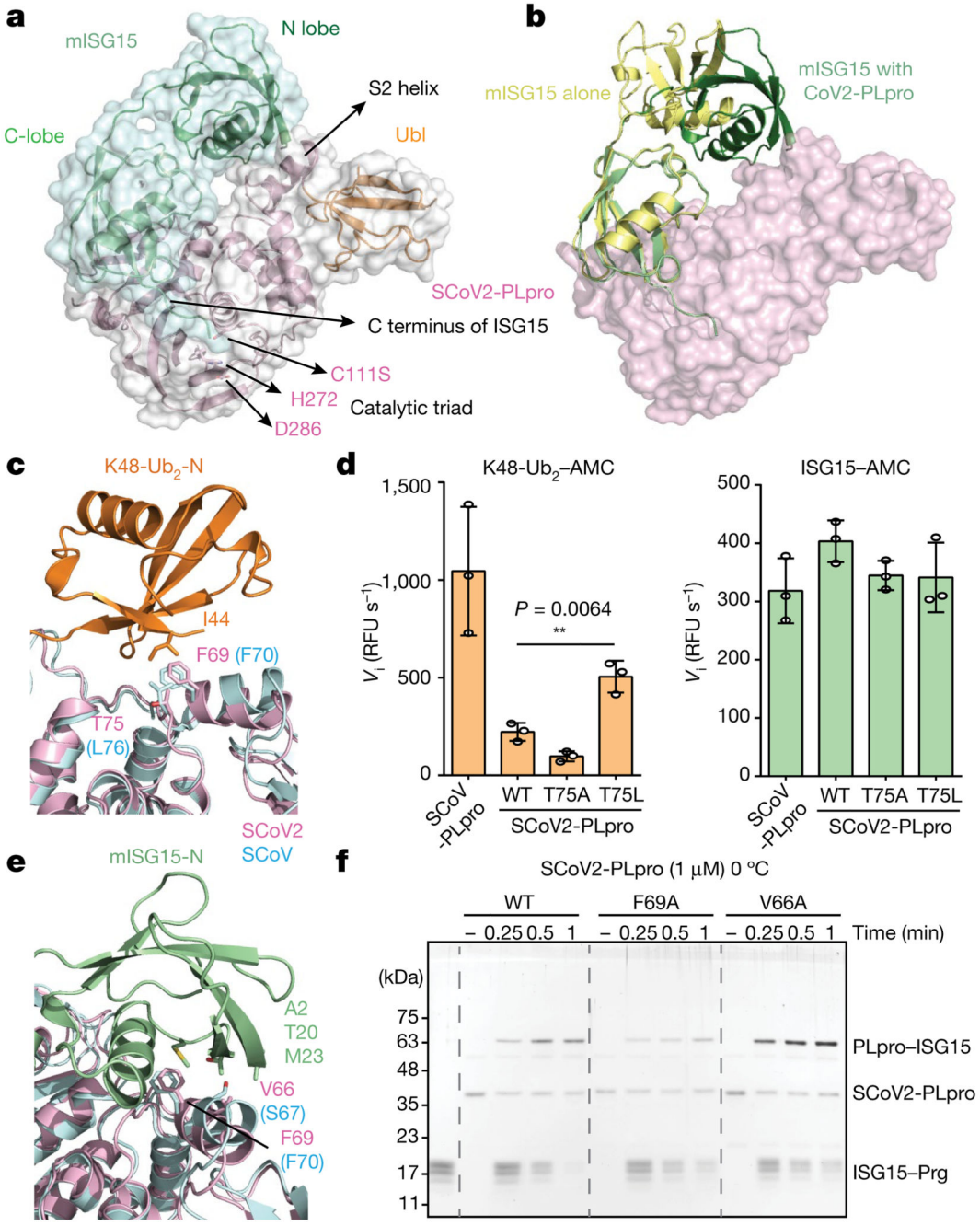

Fig. 2. Structural analysis of SARS-CoV-2 PLpro in complex with full length ISG15.

a, Crystal structure of SARS-CoV-2 PLpro(C111S) in complex with mouse ISG15. The C-terminal glycine of ISG15 and catalytic triad of SCoV2-PLpro are highlighted as stick model. The ubiquitin like domain (Ubl) is coloured orange. **b**, Comparison of unbound form of ISG15 with ISG15 in complex with SCoV2-PLpro. **c**, Comparison of N-terminal half of K48-linked di-ubiquitin (K48 Ub_2-N)–SCoV-PLpro complex structure (PDB ID: 5E6J) with ISG15–SCoV2-PLpro. Residues forming hydrophobic interactions are highlighted as stick model. **d**, Initial velocity (V_i) of AMC release from AMC probes (K48-Ub_2–AMC and

ISG15–AMC) with the indicated wild-type (WT) and mutant PLpro. Data are mean ± s.d. (n = 3 independent experiments). $^{**}P < 0.01$; two-tailed paired t-test. **e**, Comparison of N-terminal half of mouse ISG15 (ISG15-N) and SCoV2-PLpro and SCoV-PLpro (PDB ID:5E6J). Residues forming hydrophobic interactions are highlighted as stick model. **f**, ISG15–Prg was incubated with wild type and mutant SCoV2-PLpro. Experiments were repeated three times independently with similar results.

Europe PMC Funders Author Manuscripts

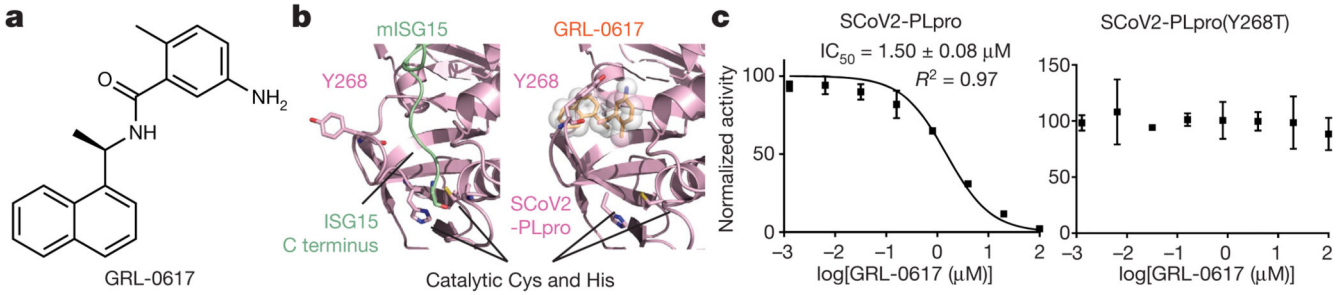

Fig. 3. Effect of GRL-0617 on SCoV2-PLpro.

a, Structure of GRL-0617. **b**, Comparison of ISG15-bound (left) and GRL-0617 bound (right) structure. Blocking loop 2 (BL2 loop) of SCoV2-PLpro is modelled on the basis of GRL-0617 bound SCoV-PLpro and SCoV2-PLpro structures (PDB ID: 3E9S[18] and 6W9C). GRL-0617-interacting Tyr268 and catalytic Cys. His residues are highlighted as stick model. **c**, Cleavage of ISG15–AMC was measured and normalized to DMSO control. IC_{50} value of GRL-0617 in relation to SCoV2-PLpro activity is presented. Data are mean ± s.d. $n = 3$ independent experiments.

Europe PMC Funders Author Manuscripts

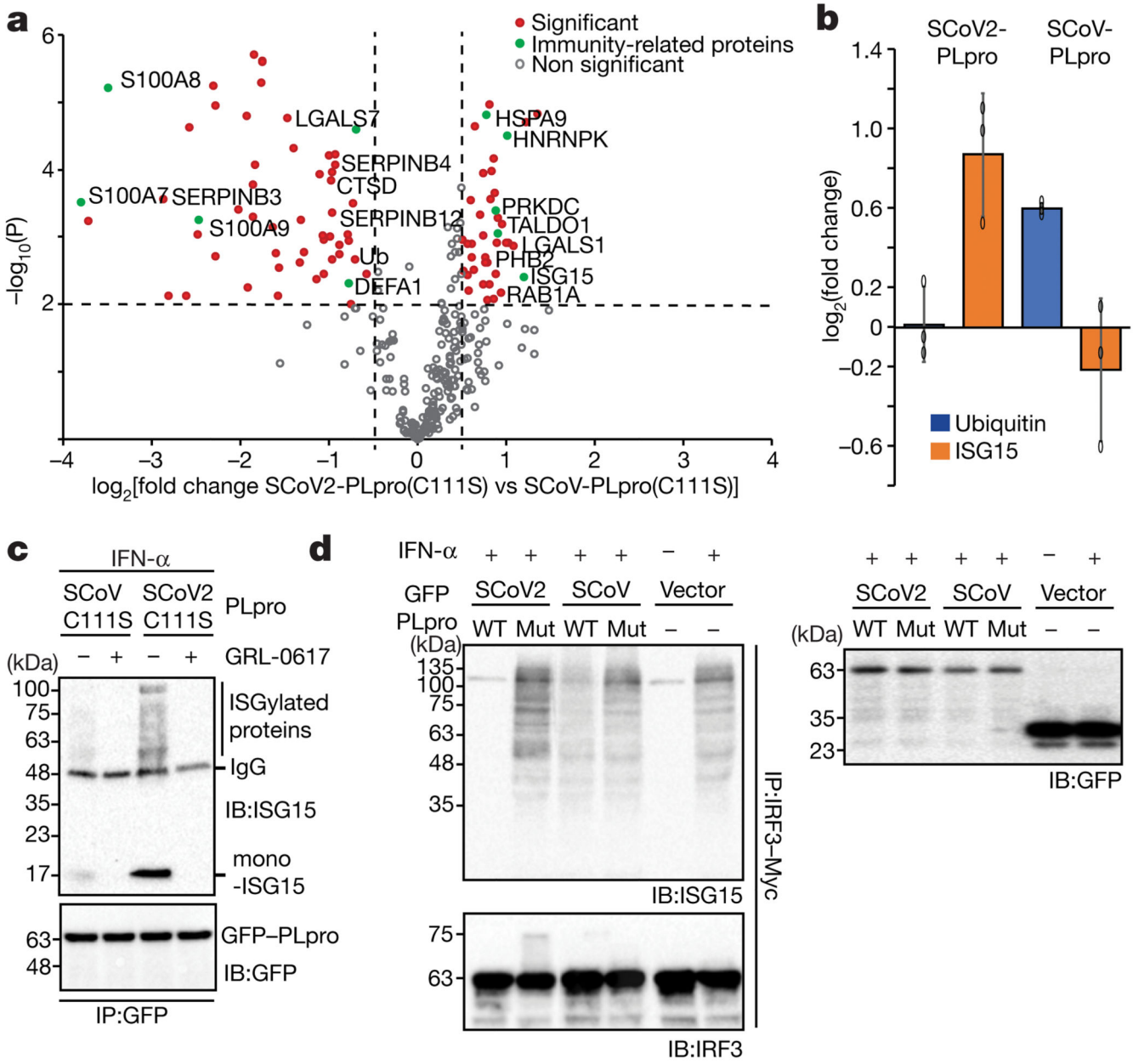

Fig. 4. Effect on PLpros on IFN and NF-κB pathways.

a, Interactome analysis comparing SCoV2-PLpro(C111S) and SCoV-PLpro(C111S). Statistically significant and immunity-related proteins are highlighted. **b**, $\log_2$(fold change) of ubiquitin and ISG15 proteins enriched by SCoV2-PLpro or SCoV-PLpro immunoprecipitates versus empty vector. Data are mean ± s.d. (n = 3, independent experiments). **c**, ISGylated proteins were enriched from A549 cells treated with IFN-α (200 U ml^{-1}) by immunoprcipitation of the indicated C111S mutant PLPro. **d**, ISGylation level of Myc–IRF3 in A549 cells expressing the indicated GFP–PLpro. Experiments in **c**, **d**, were repeated three times independently with similar results.

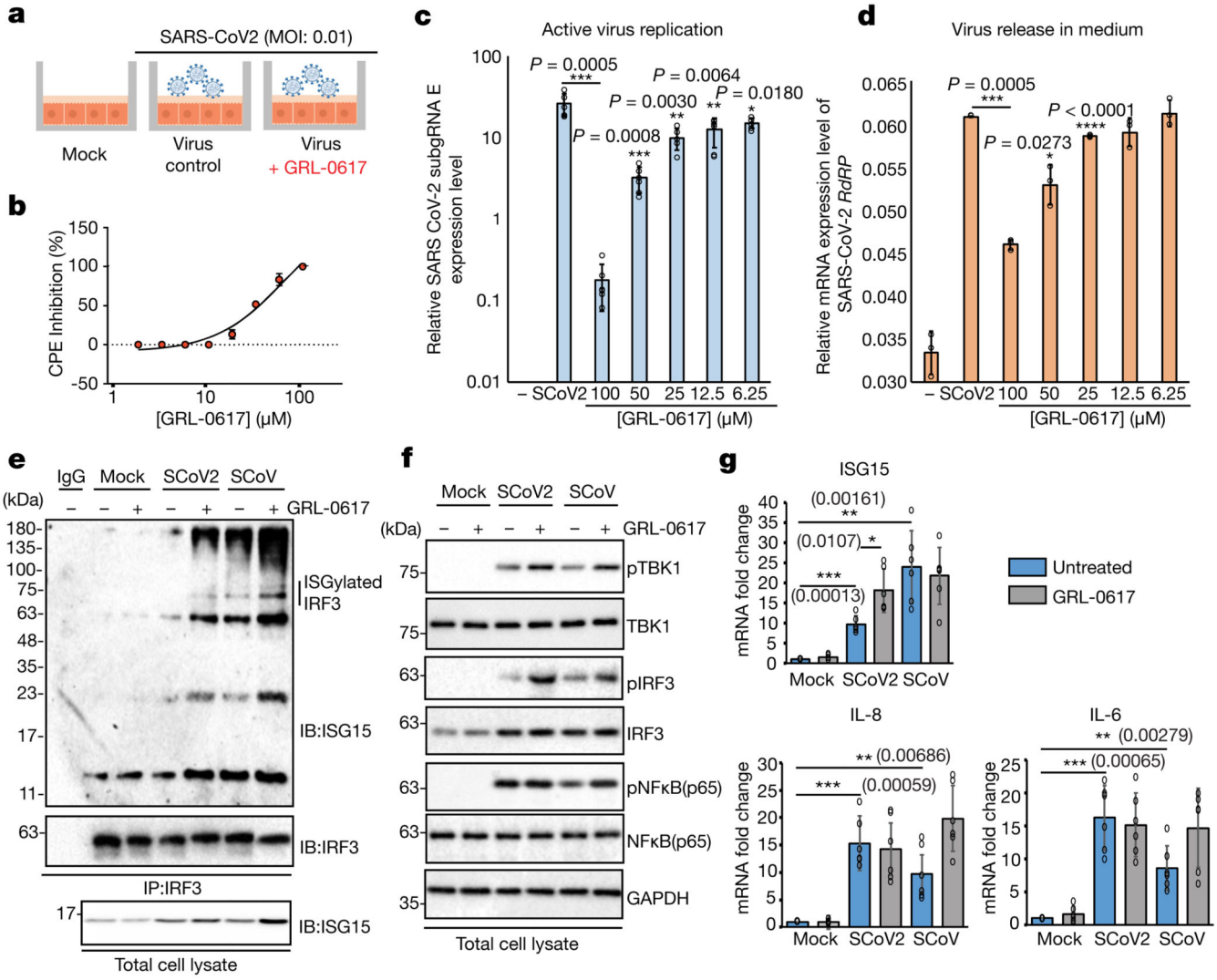

Fig. 5. Inhibitory effects of GRL-0617 on SARS-CoV2.

a, Schematic representation of the SARS-CoV-2 (strain FFM1) growth inhibition test with GRL-0617. MOI, multiplicity of infection. **b**, CPE inhibition rate of GRL-0617 on CaCo-2 cells infected with SARS-CoV2. **c**, Intracellular active virus replication was analysed by measuring SARS-CoV-2 subgenomic RNA (subgRNA E) level and normalized to the cellular *ACTB* gene. **d**, Release of viral particles in culture medium was analysed by PCR targeting the open reading frame of the RNA-dependent RNA polymerase (*RdRP*) gene of SARS-CoV-2. **e**, **f**, The effect of GRL-0617 on the type I IFN pathway. CaCo-2 cells were infected with SARS-CoV-2 or SARS-CoV with or without GRL-0617 (50 μM). pTBK1, phosphorylated TBK1; pIRF3, phosphorylated IRF3; pNF-κB p65, phosphorylated pNF-κB p65. **e**, Endogenous IRF3 was immunoprecipitated and analysed by immunoblotting. **f**, Phosphorylation of TBK1 was analysed by immunoblotting. **g**, Relative mRNA levels of indicated genes from infected cells with or without GRL-0617 (25 μM) treatment were analysed and normalized to 18S RNA. *P* values in parentheses. Data in **c**, **d**, **g**, are mean ± s.d.; $n = 3$ independent experiments. *$P < 0.05$, **$P < 0.01$, ***$P < 0.001$, ****$P < 0.0001$;

two-tailed paired *t*-test. Experiments in **e**, **f**, were repeated three times independently with similar results.

Europe PMC Funders Author Manuscripts